https://doi.org/10.5194/essd-2026-678
Preprint. Discussion started: 16 November 2026
© Author(s) 2026. CC BY 4.0 License.



Open Access Earth System Science Data Discussions

A global 0.05° dataset of daily latent heat flux and resistances (2001–2020) derived via the Energy-Resistance-Coupling framework

Lingfei Zhang[1,2], Xiaowei Wang[1,3], Yazhen Jiang[1,4*], Shuqing Wang[2], Menglin Si[1,4], Cheng Huang[5]

1. State Key Laboratory of Resources and Environmental Information System, Institute of Geographic Sciences and Natural Resources Research, Chinese Academy of Sciences, Beijing 100101, China.
2. School of Land Science and Technology, China University of Geosciences (Beijing), Beijing 100083, China.
3. School of Ecology and Applied Meteorology, Nanjing University of Information Science & Technology, Nanjing 210044, China.
4. University of Chinese Academy of Sciences, Beijing 100049, China.
5. Institute of Grassland Research, Chinese Academy of Agricultural Sciences, Hohhot 010010, China

** Authors to whom correspondence should be addressed: jiangyz@lreis.ac.cn*

Abstract. Latent heat flux (*LE*) is a key component of land surface energy partitioning and plays a critical role in regulating terrestrial water–carbon interactions and land–atmosphere feedback. Accurate quantification of *LE* depends critically on reliable estimates of effective aerodynamic resistance (r_{ae}) and surface resistance (r_s), which regulate turbulent transport and surface water vapor transfer. However, existing large-scale *LE* estimation frameworks often rely on empirical or prescribed resistance parameterizations, and most global products provide only final flux estimates while lacking long-term, spatially continuous datasets of r_{ae} and r_s. To address these limitations, we produced a spatiotemporally continuous global dataset at 0.05° resolution for 2001–2020, including *LE*, r_{ae}, r_s, the decoupling coefficient (Ω), and maximum surface relative humidity ($h_{s,max}$) by an energy- resistance-coupling (ERC) iterative framework based on multi-source remote sensing, reanalysis, and flux observations. The framework integrates (i) an aerodynamic temperature (T_0) calibration scheme, (ii) an XGBoost-based dynamic constraint on the $h_{s,max}$ and (iii) a Newton–Raphson solver to obtain a physically constrained nonlinear solution for the resistance network and latent heat flux. Validation against 244 flux sites showed good agreement between ERC *LE* and site observations, with an overall R^2 of 0.76 and RMSE of 23.54 W m^{-2}; the XGBoost-estimated $h_{s,max}$ also performed well, with a R^2 of 0.91, and an RMSE of 0.06, while the derived r_{ae}, r_s and Ω exhibited physically consistent spatial gradients and seasonal dynamics. This dataset provides a new global high-resolution source of resistance-related variables and can support drought monitoring, land–atmosphere coupling analyses, and the evaluation of Earth system models.

https://doi.org/10.5194/essd-2026-678
Preprint. Discussion started: 16 November 2026
© Author(s) 2026. CC BY 4.0 License.



Open Access Earth System Science Data Discussions

1 Introduction

Latent heat flux (*LE*) plays an important role in terrestrial water and energy exchanges. The associated evapotranspiration returns approximately 60% of global terrestrial precipitation to the atmosphere, while LE accounts for more than half of the available surface energy (Brutsaert, 2013; Oki and Kanae, 2006). Ongoing climate warming has been accompanied by increasingly frequent droughts and heatwaves. These hydroclimatic changes have been investigated by Humphrey et al. (2021), Mazdiyasni and AghaKouchak (2015), and Seneviratne et al. (2010). Reliable global LE estimates are therefore important for climate prediction and water-resource management, as discussed by Sheffield et al. (2012), Wang and Dickinson (2012), and Zhao and Running (2010).

Over the past few decades, large-scale *LE* estimation has evolved into several major methodological frameworks and global products. Thermal-infrared energy-balance models represent a major group of *LE* estimation approaches. These methods estimate LE as the residual of the surface energy balance, using land surface temperature, radiation, vegetation characteristics, and aerodynamic conditions to constrain energy partitioning. Representative implementations include SEBAL (Bastiaanssen et al., 1998), METRIC (Allen et al., 2007), SEBS (Su, 2002), SSEBop (Senay et al., 2013), ALEXI/DisALEXI, and TSEB. Anderson et al. (1997) introduced the ALEXI model, from which DisALEXI was developed as an extension. Norman et al. (1995) described the two-source approach underlying TSEB. The Priestley–Taylor formulation (Priestley and Taylor, 1972) provides the theoretical basis for this category of evaporation models. Its applications include PT-JPL (Fisher et al., 2008) and GLEAM (Miralles et al., 2011; Martens et al., 2017), which incorporate environmental constraints such as soil moisture and vegetation conditions. The Penman–Monteith approach (Penman, 1948; Monteith, 1965a) provides the theoretical foundation for several widely used global products. Examples include MOD16 (Mu et al., 2011) and the PML/PML-V2 series (Zhang et al., 2016, 2019). These models explicitly account for available energy, vapor pressure deficit, aerodynamic transport, and canopy or surface conductance. In addition, land-surface reanalysis and climatic water-balance products, such as ERA5-Land (Muñoz-Sabater et al., 2021) and TerraClimate (Abatzoglou et al., 2018), provide spatially and temporally continuous *LE* estimates through land surface model simulations or water-balance constraints. More recently, FLUXCOM has applied machine-learning techniques to upscale eddy-covariance measurements by integrating tower observations with satellite-derived information and meteorological variables, thereby generating global *LE* estimates (Jung et al., 2019). Together, these approaches have greatly advanced large-scale *LE* estimation, yet uncertainties remain in aerodynamic resistance, surface and canopy conductance, water-stress representation, and energy closure, especially under heterogeneous and moisture-limited conditions.

Although numerous global *LE* products have been developed, most of them provide only final flux estimates (Fisher et al., 2017), while resistance-related diagnostic variables are rarely released as long-term, spatially continuous datasets, limiting the diagnosis of land-atmosphere coupling, vegetation water regulation, and ecohydrological feedbacks under climate extremes (Gentine et al., 2019). Two resistance variables are particularly important for diagnosing surface–atmosphere exchange. Aerodynamic resistance (r_{ae}) characterizes turbulent transfer between the land surface and the overlying air. Surface resistance

https://doi.org/10.5194/essd-2026-678
Preprint. Discussion started: 16 November 2026
© Author(s) 2026. CC BY 4.0 License.



Open Access Earth System Science Data Discussions

(r_s), in contrast, represents the restrictions associated with stomatal activity, soil evaporation, and moisture availability near the surface (Kelliher et al., 1995; Mahrt, 1996). However, these variables remain poorly represented in current global products, many existing models still estimate r_s using empirical schemes driven by vapor pressure deficit, soil moisture, radiation, or temperature. Examples of these parameterizations are discussed by Jarvis (1976) and Ball et al. (1987). Related formulations were also presented by Stewart (1988) and Collatz et al. (1991). Under pronounced thermal or moisture stress, empirical schemes may produce resistance estimates beyond plausible physiological or physical limits. Related limitations have been discussed by Foken (2008) and Novick et al. (2016). Further evidence is reported in the studies of Yuan et al. (2019) and Zhou et al. (2019). Therefore, constructing a physically constrained *LE* dataset that simultaneously provides both flux estimates and key resistance variables is essential for moving beyond endpoint flux retrieval toward mechanism-oriented land surface diagnostics (Wang et al., 2026).

To address the lack of long-term, spatially continuous resistance-related products, we generated a global 0.05° dataset of LE and resistance variables for the period 2001–2020. We implemented an iterative Energy–Resistance–Coupling (ERC) framework that integrates satellite-derived surface information with meteorological fields from reanalysis products. The framework jointly constrains the resistance network and latent heat flux (*LE*) within an explicit surface energy balance formulation that incorporates land–atmosphere coupling (Ω), with the maximum surface relative humidity ($h_{s,max}$) serving as the linking variable that bounds the solution space. The datasets were evaluated against 244 flux tower sites. By providing globally consistent estimates of both fluxes and resistance-related variables, this dataset fills a critical gap in high-resolution global resistance products and supports future studies of land–atmosphere interactions, drought monitoring, and carbon–water cycle dynamics in a change climate.

2 Data

The input collection comprises three main components: satellite remote sensing products, meteorological reanalysis data, and in-situ flux observations. These inputs are used to develop a global 0.05° dataset of land surface energy and resistance variables covering 2001–2020.

2.1 Multi-source satellite remote sensing data

The ERC framework drew on optical and thermal-infrared satellite products to characterize surface conditions and vegetation properties (Table 1). Daily land surface temperature (T_s) was taken from the 1-km all-weather product developed by Li et al. (2024), which provides global daily mean estimates derived from MODIS observations. Vegetation status were represented by daily MODIS NDVI product (MCD19A3CMG; Lyapustin, 2023) and the 8-day GLASS LAI product (Ma et al., 2022; Ma and Liang, 2022). GLASS LAI complemented NDVI by supplying information on canopy structure. To retain this information at the daily time step, we linearly interpolated the 8-day LAI observations to daily values. The relatively few missing observations in the GLASS record also helped maintain continuity in the vegetation inputs. Annual land-cover classes were

https://doi.org/10.5194/essd-2026-678
Preprint. Discussion started: 16 November 2026
© Author(s) 2026. CC BY 4.0 License.



obtained from MODIS MCD12C1 (Friedl and Sulla-Menashe, 2022). Prior to data integration, the input layers were harmonized to the target 0.05° spatial grid through projection adjustment and resampling.

Table 1: Satellite remote sensing products used in the ERC framework

Dataset	Product or data source	Spatial resolution	Temporal resolution	Role in the ERC framework	Reference
Land surface temperature, T_s	Global all-weather daily mean LST product	1 km	Daily	Thermal input for constraining surface energy exchange	Li et al. (2024)
Normalized Difference Vegetation Index, NDVI	MODIS MCD19A3CMG daily NDVI product	0.05°	Daily	Characterization of vegetation greenness and condition	Lyapustin (2023)
Leaf Area Index, LAI	GLASS LAI product	0.05°	8-day	Canopy-structure information with continuous temporal coverage and few missing observations	Ma et al. (2022); Ma and Liang·(2022)
Land cover type	MODIS MCD12C1 Land Cover Type product	0.05°	Annual	Land-cover classes for model-parameter assignment and surface-type grouping	Friedl and Sulla-Menashe (2022)

2.2 Meteorological reanalysis data

Atmospheric forcing was taken from ERA5-Land (Muñoz-Sabater et al., 2021). The meteorological fields used in the analysis were R_n, T_a and T_d (both measured at 2 m), P_a, and WS obtained at a height of 10 m. The $h_{s,max}$ prediction additionally drew on precipitation, snow depth, and soil water content measured in the 0–7 and 7–28 cm layers. Before integration with the satellite products, the native 0.1° ERA5-Land fields were bilinearly interpolated onto the 0.05° grid.

2.3 In-situ flux tower observations

Globally distributed eddy covariance (EC) observations were used both as reference data for model training and as independent data for product evaluation. The compiled observations originated from several networks, including AmeriFlux (Novick et al., 2018), ChinaFLUX (Yu et al., 2006), and OzFlux (Beringer et al., 2016), together with EuroFlux, FLUXNET, and TPDC. The FLUXNET data-processing framework is described by Pastorello et al. (2020). The screening process yielded 244 flux-tower sites suitable for subsequent product evaluation, based on the completeness and reliability of their observations. These sites cover major bioclimatic zones and represent 11 land-cover types classes defined by the IGBP classification scheme (Figure 1). A quality-control procedure was applied to the raw half-hourly or hourly observations. Records during precipitation events and the immediately adjacent periods were excluded, and data with poor quality control (QC) flags or physically unrealistic outliers were removed. The remaining observations were aggregated to daily values. Three key quantities were extracted from the EC measurements: latent heat flux (LE), sensible heat flux (H), and available energy ($R_n - G$). During $h_{s,max}$ model

https://doi.org/10.5194/essd-2026-678
Preprint. Discussion started: 16 November 2026
© Author(s) 2026. CC BY 4.0 License.



development, XGBoost was fitted using observations from a designated group of flux towers; data collected at the other sites formed the independent test set.

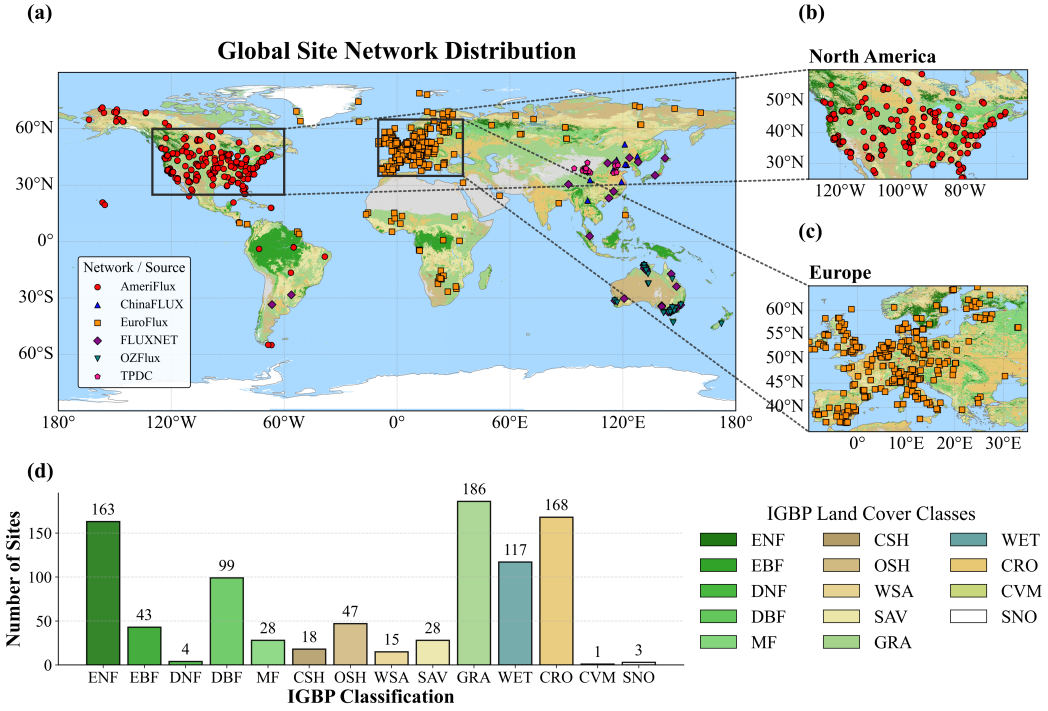
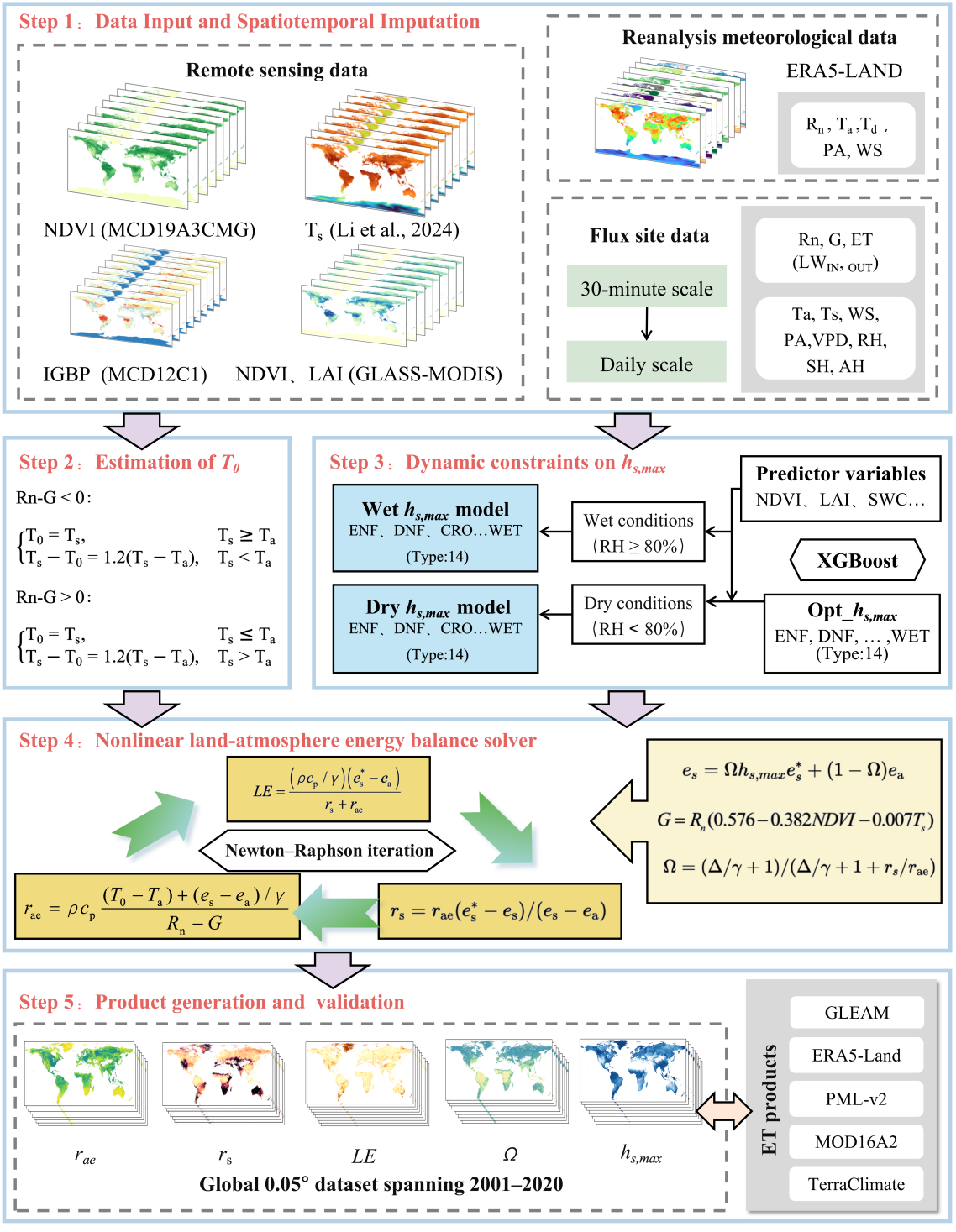


Figure 1: Spatial coverage and IGBP composition of the 244 eddy-covariance sites used in this study. (a) Global distribution of the selected sites; (b) enlarged view of North America; (c) enlarged view of Europe; (d) number of sites in each IGBP land-cover class.

3 Methodology

To generate a global, spatially continuous dataset of LE and resistance-related variables, we implemented an Energy–Resistance–Coupling (ERC) iterative framework within a surface energy balance formulation. The ERC framework links LE, resistances, and land–atmosphere coupling through a set of nonlinear equations, thereby providing the methodological basis for deriving LE, r_{ae}, r_s, Ω and $h_{s,max}$ as coherent daily products (Wang et al., 2026). Figure 2 summarizes the workflow used to generate the global dataset, including (1) preprocessing of remote sensing, reanalysis, and flux data; (2) calibration of aerodynamic temperature (T_0); (3) prediction of $h_{s,max}$; (4) derivation of r_{ae}, r_s, and Ω; and (5) calculation and evaluation of LE. After input data preprocessing (Step 1), T_0 is first calculated from T_s, T_a, and the surface energy state (Step 2). Then $h_{s,max}$ is predicted with XGBoost model using multi-source observations and a humidity-stratified training strategy (Step 3; Chen and Guestrin, 2016). At Step 4, we apply the Newton–Raphson method to iteratively solve the coupled equations and derive physically consistent estimates of LE, r_{ae}, r_s, and Ω. Finally, the daily products are evaluated with in-situ datasets and intercompared with other products (Step 5).

https://doi.org/10.5194/essd-2026-678
Preprint. Discussion started: 16 November 2026
© Author(s) 2026. CC BY 4.0 License.



130 **Figure 2: The workflow for the production and validation of the global 0.05° land surface latent heat flux and resistance datasets.**

https://doi.org/10.5194/essd-2026-678
Preprint. Discussion started: 16 November 2026
© Author(s) 2026. CC BY 4.0 License.



Open Access Earth System Science Data Discussions

3.1 Aerodynamic temperature calibration

T_0 is calibrated prior to solving the resistance equations, because the radiometric surface temperature does not always represent the effective temperature governing turbulent heat exchange. Following Choudhury et al. (1986) and Choudhury and Monteith (1986), T_0 was adjusted based on atmospheric stability and the sign of available energy (Eq. (1)). The calibrated T_0 is then used in the subsequent energy partitioning calculation.

$$\begin{cases} T_0 = T_s, & (T_s \geq T_a) \\ T_s - T_0 = 1.2(T_s - T_a), & (T_s < T_a) \end{cases}, \text{When } R_n - G < 0$$

$$\begin{cases} T_0 = T_s, & (T_s \leq T_a) \\ T_s - T_0 = 1.2(T_s - T_a), & (T_s > T_a) \end{cases}, \text{When } R_n - G > 0 \quad (1)$$

3.2 Machine learning estimation of maximum surface relative humidity ($h_{s,max}$)

This study introduces $h_{s,max}$, which represents the upper limit of relative humidity within near-surface pores or stomatal spaces at a given land surface temperature, as a constraint on surface evaporation conditions. An XGBoost model was trained to predict $h_{s,max}$ from multi-source inputs (Wang et al., 2025). During model development, feature importance was evaluated, and for each IGBP land cover type, the ten highest-ranking predictors are retained in the final model configuration (Eq. (2)). To account for differences between moisture-abundant and moisture-stressed conditions, the training samples are further divided into high-humidity and low-humidity subsets using an air relative humidity threshold of 80%. This humidity-stratified modeling strategy allowed $h_{s,max}$ to respond differently under wet and dry conditions.

$$h_{s,max} = f_{XGB}(T_s, T_a, WS, VPD, NDVI, P_a, P_{rec}, G, SD, SWC_1, SWC_2, RH, R_n, LAI) \quad (2)$$

where f_{XGB} represents the trained XGBoost model. The predictors cover several categories of environmental information. Thermal and atmospheric conditions are characterized by T_s (land surface temperature), T_a (air temperature), P_a (atmospheric pressure), RH (relative humidity), and VPD (vapor pressure deficit). Meteorological and energy-related inputs comprise WS (wind speed), P_{rec} (precipitation), R_n (net radiation), and G (soil heat flux). Vegetation and surface-state information is represented by NDVI (normalized difference vegetation index), LAI (leaf area index), and SD (snow depth). In addition, SWC_1 and SWC_2 describe soil water content at depths of 0–7 and 7–28 cm, respectively.

3.3 Nonlinear land-atmosphere energy balance solver

The ERC solver obtains r_{ae} and r_s simultaneously while enforcing the surface energy balance, aerodynamic temperature constraints, and vapor-pressure relationships. Equation (3) links r_{ae} to three physical quantities: available energy (R_n - G), the temperature contrast between T_0 and T_a, and the vapor-pressure gradient connecting the effective surface state with ambient air. Equation (4) subsequently links r_s to r_{ae} through the quotient of two vapor-pressure gaps, namely (e_s^* − e_s) and (e_s − e_a).

https://doi.org/10.5194/essd-2026-678
Preprint. Discussion started: 16 November 2026
© Author(s) 2026. CC BY 4.0 License.



Open Access Earth System Science Data Discussions

$$r_{ae} = \frac{\rho c_p \left(T_0 - T_a\right) + \left(e_s - e_a\right)/\gamma}{R_n - G} \tag{3}$$

$$r_s = r_{ae} \frac{e_s^* - e_s}{e_s - e_a} \tag{4}$$

r_{ae} denotes the resistance governing turbulent heat and water-vapor transfer between the effective evaporating surface and the reference atmosphere. ρ and c_p denote the density of air and its heat capacity under constant-pressure conditions, respectively. T_0 and T_a refer to aerodynamic and air temperature, while e_s and e_a denote effective surface and actual air vapor pressure. The psychrometric constant is denoted by γ, whereas e_s^* refers to the saturation vapor pressure corresponding to T_0.

In addition, Ω, as proposed by McNaughton and Jarvis (1983), provides a useful measure of land–atmosphere coupling by linking the resistance network to atmospheric vapor pressure deficit. It quantifies whether LE is primarily controlled by available energy or by aerodynamic and surface resistance constraints (Bruin, 1983; Pereira, 2004; Ershadi et al., 2014). In this study, Ω is calculated from the converged resistance terms following the McNaughton–Jarvis formulation. The relationship among Ω, r_{ae} and r_s is written in Eq. (5):

$$\Omega = \frac{\Delta/\gamma + 1}{\Delta/\gamma + 1 + r_s/r_{ae}} \tag{5}$$

In Eq. (5), Δ describes the temperature dependence of saturation vapor pressure, and γ denotes the psychrometric constant. A larger Ω indicates that LE is more strongly controlled by available energy and that the surface is relatively decoupled from atmospheric aerodynamic demand, and vice versa.

LE is estimated using the vapor-gradient form of the resistance equation, and its final expression is written in Eq. (6) (Monteith, 1965b; Penman, 1948):

$$LE = \frac{\left(\rho c_p/\gamma\right)\left(e_s^* - e_a\right)}{r_s + r_{ae}} \tag{6}$$

The LE estimate is obtained from the resistance network subject to the physical constraints of the ERC framework. In this process, r_{ae} and r_s are derived under the constraints of aerodynamic temperature, maximum surface relative humidity, energy balance, and vapor-pressure gradients. This treatment ensures that the retrieved LE is compatible with the energy-balance formulation and the underlying land–atmosphere exchange processes. Equations (3)– (6) form a system of equations, which is solved iteratively under physical constraints ensuring positive resistance values and thermodynamically valid vapor-pressure states. Consequently, the final ERC dataset includes LE, r_{ae}, r_s, Ω, and $h_{s,max}$.

3.4 Estimation of other intermediate variables

Three vapor-pressure terms are involved in determining r_{ae} and r_s: actual air vapor pressure (e_a), saturated vapor pressure at the aerodynamic temperature (e_s^*), and effective surface vapor pressure (e_s) (Monteith, 1965a; McNaughton and Jarvis, 1983;

https://doi.org/10.5194/essd-2026-678
Preprint. Discussion started: 16 November 2026
© Author(s) 2026. CC BY 4.0 License.



Open Access Earth System Science Data Discussions

Stewart, 1988; Boegh et al., 2002; Mallick et al., 2014). Dewpoint temperature provides the basis for calculating e_a, as expressed in Eq. (7):

$$e_a = 0.6108 \times \exp\left(\frac{17.27 \times T_d}{T_d + 237.3}\right) \quad (7)$$

where T_d is dewpoint temperature. Using the aerodynamic temperature (T_0), we calculate the corresponding saturation vapor pressure according to Eq. (8):

$$e_s^* = 0.6108 \times \exp\left(\frac{17.27 \times T_0}{T_0 + 237.3}\right) \quad (8)$$

Within the ERC formulation, e_s represents the vapor-pressure state of the effective evaporating surface. Its magnitude depends on $h_{s,max}$ and the degree of land–atmosphere coupling, as expressed in Eq. (9):

$$e_s = \Omega h_{s,max} e_s^* + (1 - \Omega) e_a \quad (9)$$

When Ω tends toward zero, e_s approaches e_a. This limiting behavior represents strong surface–atmosphere coupling, under which atmospheric conditions exert greater control over evaporation.

The resistance calculations require the net energy remaining after soil heat storage, expressed as ($R_n - G$). Soil heat flux G is estimated using the parameterization proposed by Jiang et al. (2018), with net radiation, vegetation status, and land surface temperature serving as inputs:

$$G = R_n \left(0.576 - 0.382 \times NDVI - 0.007 \times T_s\right) \quad (10)$$

R_n denotes net radiation, NDVI represents the normalized difference vegetation index, and T_s refers to land surface temperature.

3.5 Evaluation metrics and statistical analyses

We applied statistical measures to characterize dataset accuracy and examine variations across space and time. Paired valid samples refer to the records for which the ERC estimates and the corresponding reference values were both available after spatial and temporal matching. R^2 describes how closely the estimated values correspond to the reference observations. RMSE measures the magnitude of prediction errors, whereas bias indicates their systematic direction.

Standardized Z-scores are further used to compare spatial or temporal anomalies among variables with different units and magnitudes

$$Z = \frac{x - \mu}{\sigma} \quad (11)$$

In Eq. (11), x denotes the value before standardization, whereas μ and σ represent its mean and standard deviation, respectively. All metrics are calculated after removing missing, invalid, or physically unreasonable values, and the same screening criteria are applied consistently across sites, products, regions, and time periods.

https://doi.org/10.5194/essd-2026-678
Preprint. Discussion started: 16 November 2026
© Author(s) 2026. CC BY 4.0 License.



Open Access Earth System Science Data Discussions

4 Results

4.1 Evaluation of the intermediate parameters' estimation

Within the ERC framework, $h_{s,max}$ provides a dynamic constraint on the upper limit of near-surface relative humidity. Figure 3a shows close agreement between the XGBoost estimates of $h_{s,max}$ and the observation-derived values across the global flux sites, with R^2 of 0.91, RMSE of 0.06, and Bias of 0.00. Under stratified-moisture conditions, the model also maintains low absolute errors in both humidity regimes. Under high-humidity conditions (RH ≥ 80%), the RMSE is 0.04 (Fig. 3b). Under low-humidity conditions (RH < 80%), the model remains stable, with RMSE = 0.07 (Fig. 3c). These results indicate that the predicted $h_{s,max}$ is reliable across both moist and water-stressed environments. The response curves to environmental variables (RH, VPD, SWC) in Fig. 3d–f further show that the estimated $h_{s,max}$ follows physically interpretable gradients. To emphasize relative temporal variations among variables, the time-series data in Fig. 3g are standardized using Z-scores. Specifically, $h_{s,max}$ increased with increasing RH, declined with increasing VPD, and exhibited a threshold-like response to SWC. In particular, the response to SWC showed a sharp increase when SWC was below 20%, followed by gradual stabilization toward saturation. The resistance terms (r_{ae} and r_s) are evaluated with Z-score standardization across representative land cover types (Fig.4), including GRA, DBF, and ENF. In Fig. 4a, the simulated r_{ae} generally follows the Surface Temperature Initiated Closure (STIC) model-derived reference benchmark, capturing the main seasonal fluctuations and the timing of peaks and troughs. The multi-site scatter comparison in Fig. 4b further indicates that the simulated r_{ae} estimates form a narrow distribution around the identity line in Z-score space, with no obvious systematic offset. These results indicate that the ERC framework captures seasonal variability in aerodynamic resistance across heterogeneous ecosystems.

Figure 5 presents the validation of surface resistance (r_s). The representative time series in Fig. 5a show that the ERC-derived r_s follows the expected annual course: it declines during active canopy development and rises in dormant or drought-affected periods. The seasonal trajectories of the ERC estimates are closely aligned with the P–M reference benchmark at the representative sites shown. The cross-site comparison in Fig. 5b further shows that the simulated r_s estimates track the P–M reference relationship across sites. Taken together, the seasonal trajectories and site-level comparisons indicate that ERC captures changes in rs across ecosystems with differing vegetation structure and water availability.

Figure 6 compares Ω values derived from the ERC framework with those calculated using the Penman–Monteith approach. In Fig. 6a, the ERC framework captures the dominant seasonal patterns of Ω at representative ENF, DBF, GRA, and woody savanna (WSA) sites, with higher values during active canopy development and lower values during dormant or water-limited periods. In Fig. 6b, the ERC-derived Ω estimates closely follow the reference values, showing a clear positive association. The agreement shown in Fig. 6 supports not only the realism of the simulated Ω, but also the coherence of the coupled resistance solution underlying the ERC framework.

https://doi.org/10.5194/essd-2026-678
Preprint. Discussion started: 16 November 2026
© Author(s) 2026. CC BY 4.0 License.

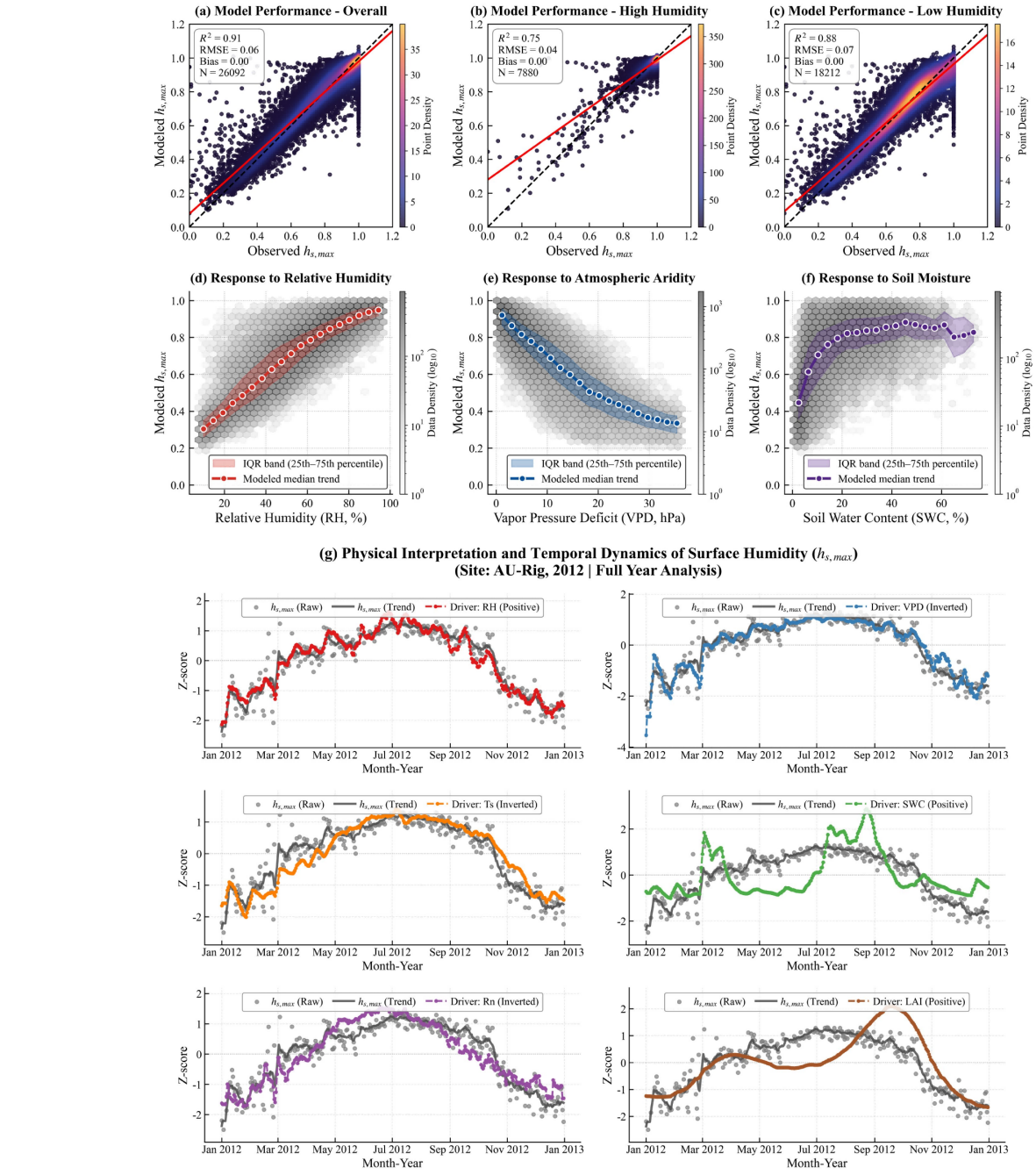


Figure 3: Accuracy validation and environmental response characteristics of $h_{s,max}$. (a–c) Scatter plots comparing simulated and observation-derived values under overall, high-humidity (RH ≥ 80%), and low-humidity (RH < 80%) conditions. (d–f) Response curves of simulated $h_{s,max}$ to relative humidity, vapor pressure deficit, and soil water content. Shaded areas represent the interquartile range.

https://doi.org/10.5194/essd-2026-678
Preprint. Discussion started: 16 November 2026
© Author(s) 2026. CC BY 4.0 License.



Open Access Earth System Science Data Discussions

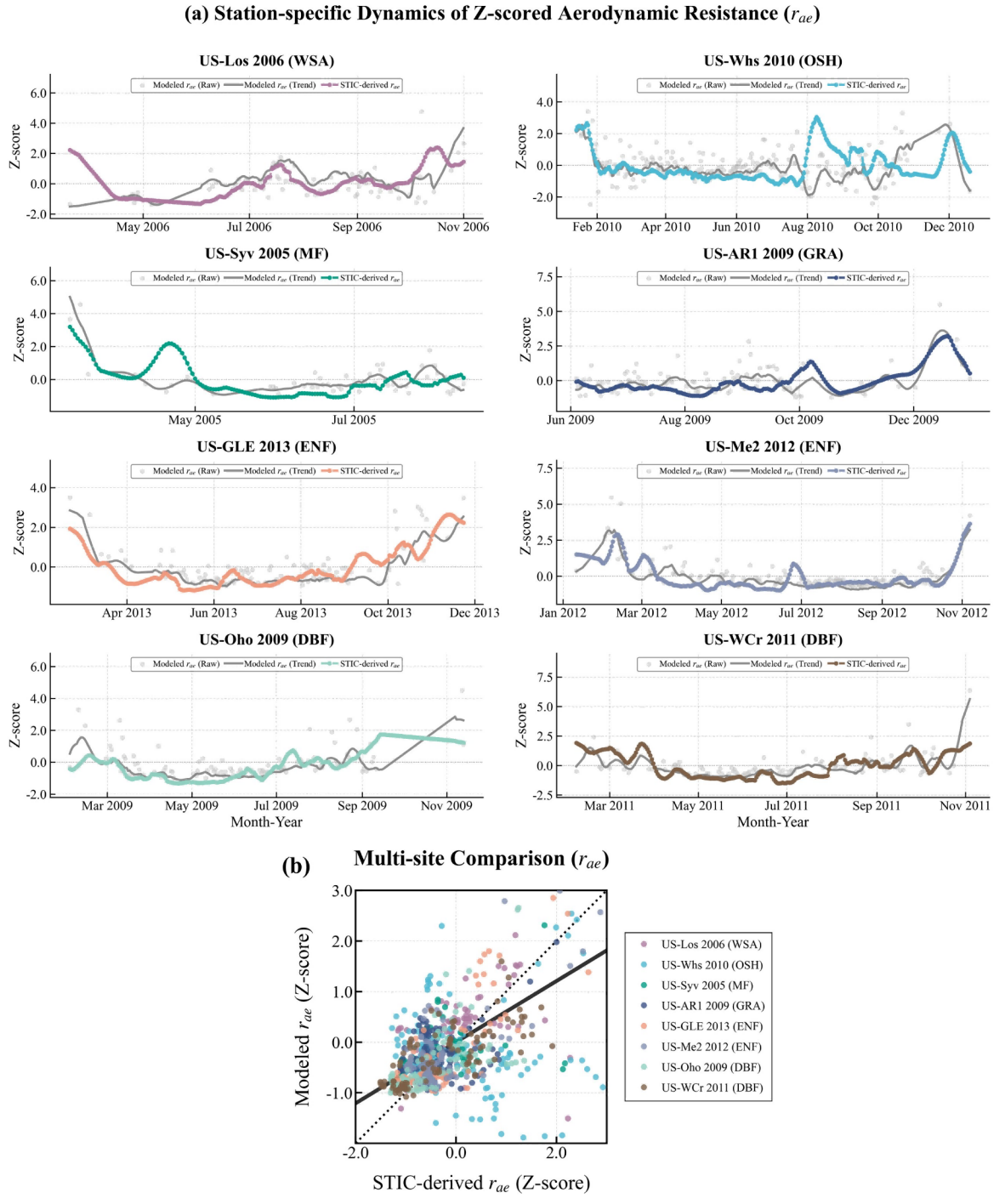


Figure 4: Temporal dynamics and multi-site validation of aerodynamic resistance (r_{ae}). (a) Z-score standardized seasonal evolution of ERC-derived r_{ae} at representative flux sites and its comparison with the STIC reference r_{ae} . (b) Scatter plot validation of simulated r_{ae} against reference values across all representative sites.

https://doi.org/10.5194/essd-2026-678
Preprint. Discussion started: 16 November 2026
© Author(s) 2026. CC BY 4.0 License.

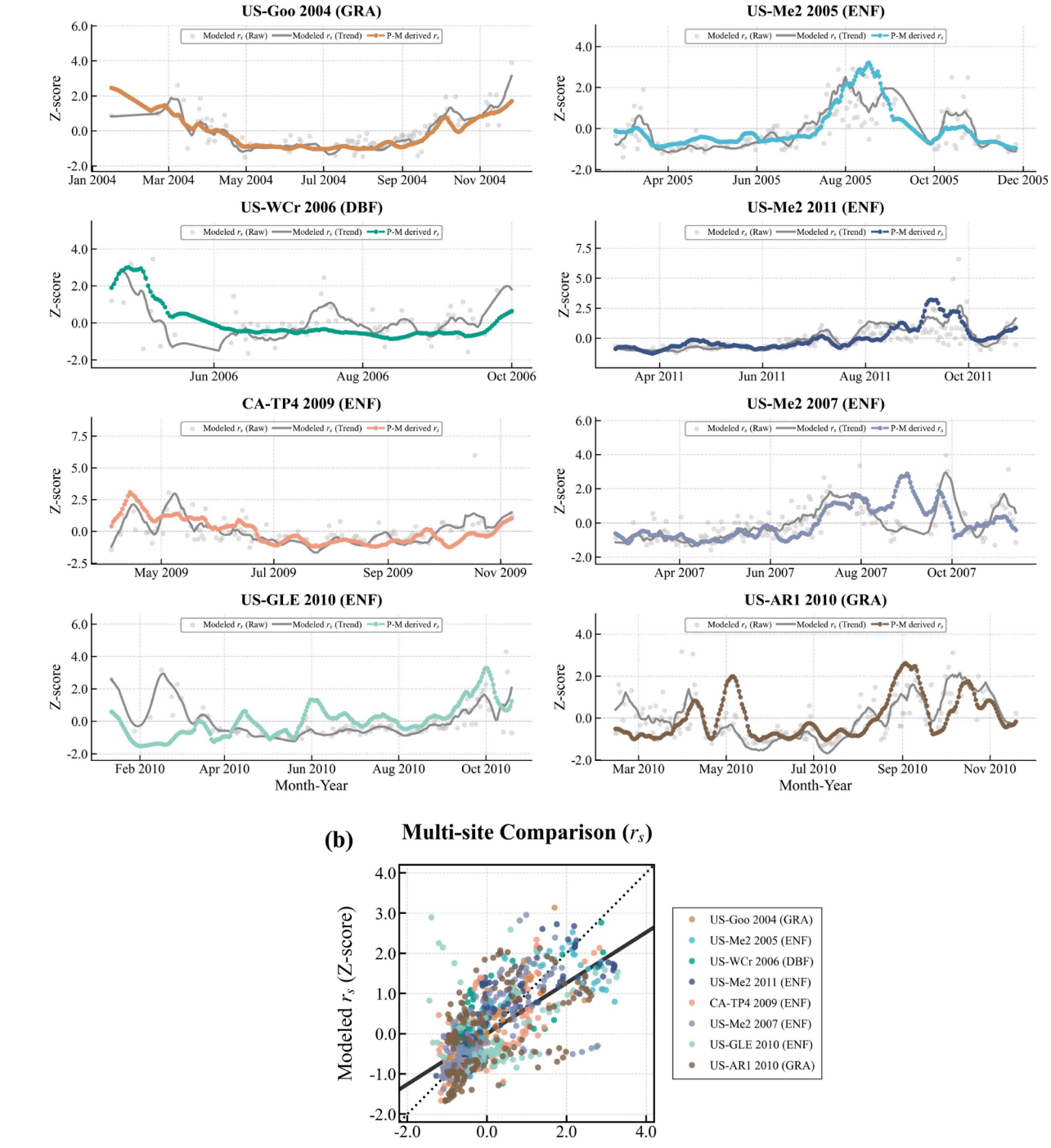
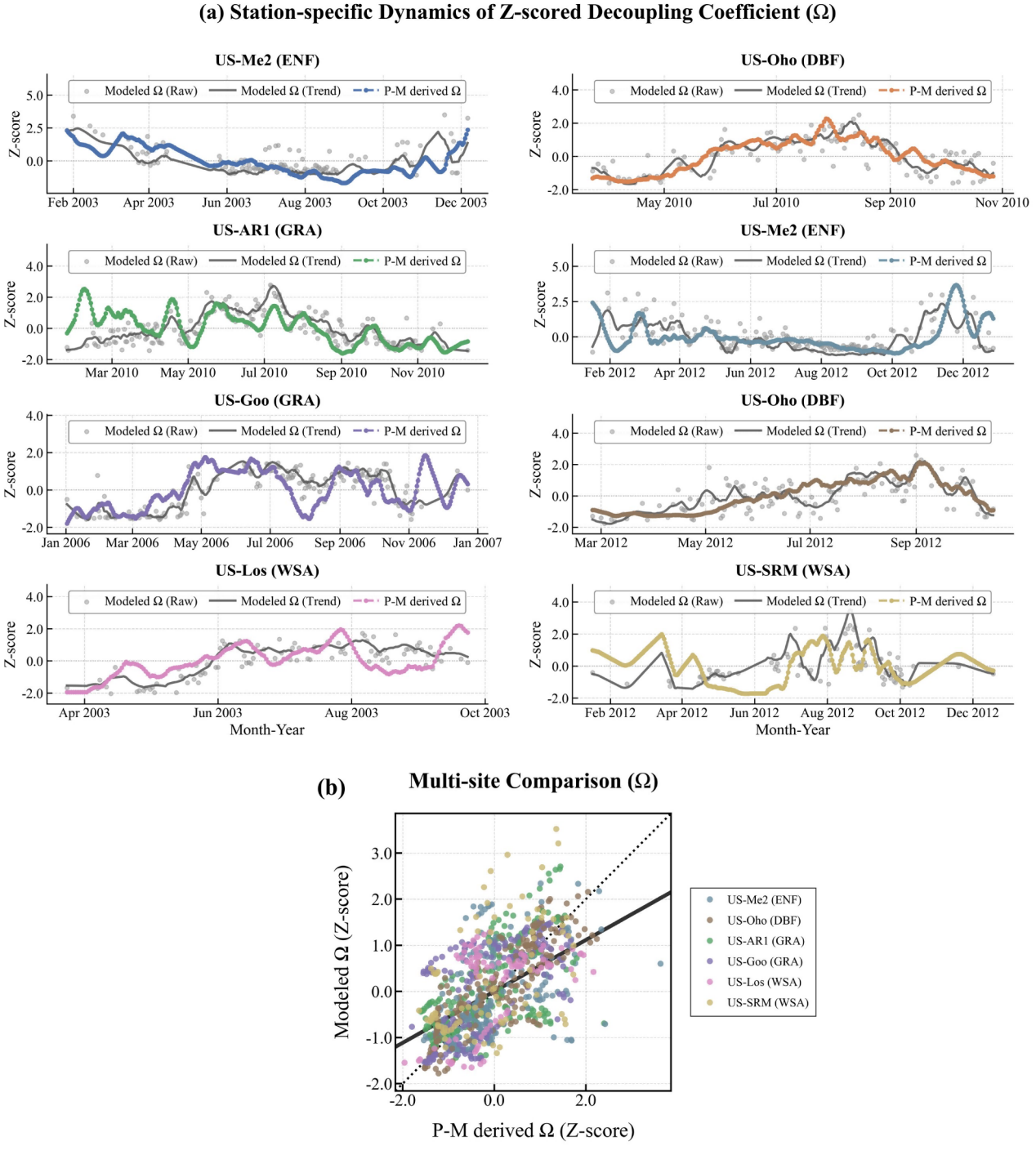


Figure 5: Temporal dynamics and multi-site validation of surface resistance (r_s). (a) Z-score standardized seasonal evolution of r_s at representative flux sites and its comparison with the Penman-Monteith (P-M) reference benchmark. (b) Scatter plot validation of simulated r_s against P-M reference values across all representative sites.

https://doi.org/10.5194/essd-2026-678
Preprint. Discussion started: 16 November 2026
© Author(s) 2026. CC BY 4.0 License.



Open Access Earth System Science Data Discussions



255

Figure 6: Temporal dynamics and multi-site validation of the decoupling coefficient (*Ω*). (a) Z-score standardized seasonal evolution of *Ω* at representative flux sites compared against the Penman–Monteith (P-M) reference benchmark. (b) Scatterplot validation of ERC-simulated Ω against P-M reference values across all representative sites.

https://doi.org/10.5194/essd-2026-678
Preprint. Discussion started: 16 November 2026
© Author(s) 2026. CC BY 4.0 License.



4.2 Accuracy assessment of latent heat flux

Section 4.2 examines the ERC-derived *LE* estimates through tower-based validation and comparisons with established global datasets (Fig. 7 and 8). The tower comparison in Fig. 7a–c yielded an overall R^2 of 0.75, accompanied by an RMSE of 23.54 W m^{-2}. The model maintained consistently robust retrieval performance across contrasting moisture regimes, achieving R^2 and RMSE were 0.74 and 24.59 W m^{-2} respectively; the corresponding statistics for the high-humidity subset were 0.76 and 20.73 W m^{-2}. At the daily timescale, the ERC model outperformed both GLEAM and ERA5-Land *LE*. Its (R^2, RMSE) values were (0.54, 29.99 W m^{-2}), while GLEAM and ERA5-Land produced (0.40, 32.12 W m^{-2}) and (0.32, 38.87 W m^{-2}), respectively. At the 8-day composite scale, ERC also showed higher accuracy than MOD16A2 and slightly better accuracy than PML-v2. As shown in Fig. 7g–i, the (R^2, RMSE) pair for ERC was (0.66, 22.64 W m^{-2}). The corresponding pairs were (0.52, 29.03 W m^{-2}) for MOD16A2 and (0.62, 23.83 W m^{-2}) for PML-v2. At the monthly scale, the advantage of ERC became more pronounced (Fig.7j–l). The (R^2, RMSE) values were (0.70, 20.06 W m^{-2}) for ERC, (0.59, 24.64 W m^{-2}) for GLEAM, and (0.46, 29.69 W m^{-2}) for TerraClimate. These multi-temporal comparisons collectively indicate that the ERC dataset exhibits strong temporal robustness and provides LE that are competitive with or superior to, several established global products.

The biome-specific validation (Figure 8) further substantiates the robust adaptability of the ERC framework to land surface heterogeneity. Overall, the model demonstrates consistent and largely unbiased estimation capabilities across a wide range of terrestrial biomes. For ecosystems characterized by relatively simple canopy structures and lower aerodynamic roughness—such as Grasslands (GRA), Woody Savannas (WSA), and Savannas (SAV)—the model exhibited minimal systematic bias , with bias estimates spanning −1.5 to 0.3 W m^{-2}; RMSE values for these classes were 28.1–30.5 W m^{-2}. These categorical validation results reinforce the capability of the ERC framework to capture LE variability across diverse land surface types with reliable accuracy.

https://doi.org/10.5194/essd-2026-678
Preprint. Discussion started: 16 November 2026
© Author(s) 2026. CC BY 4.0 License.

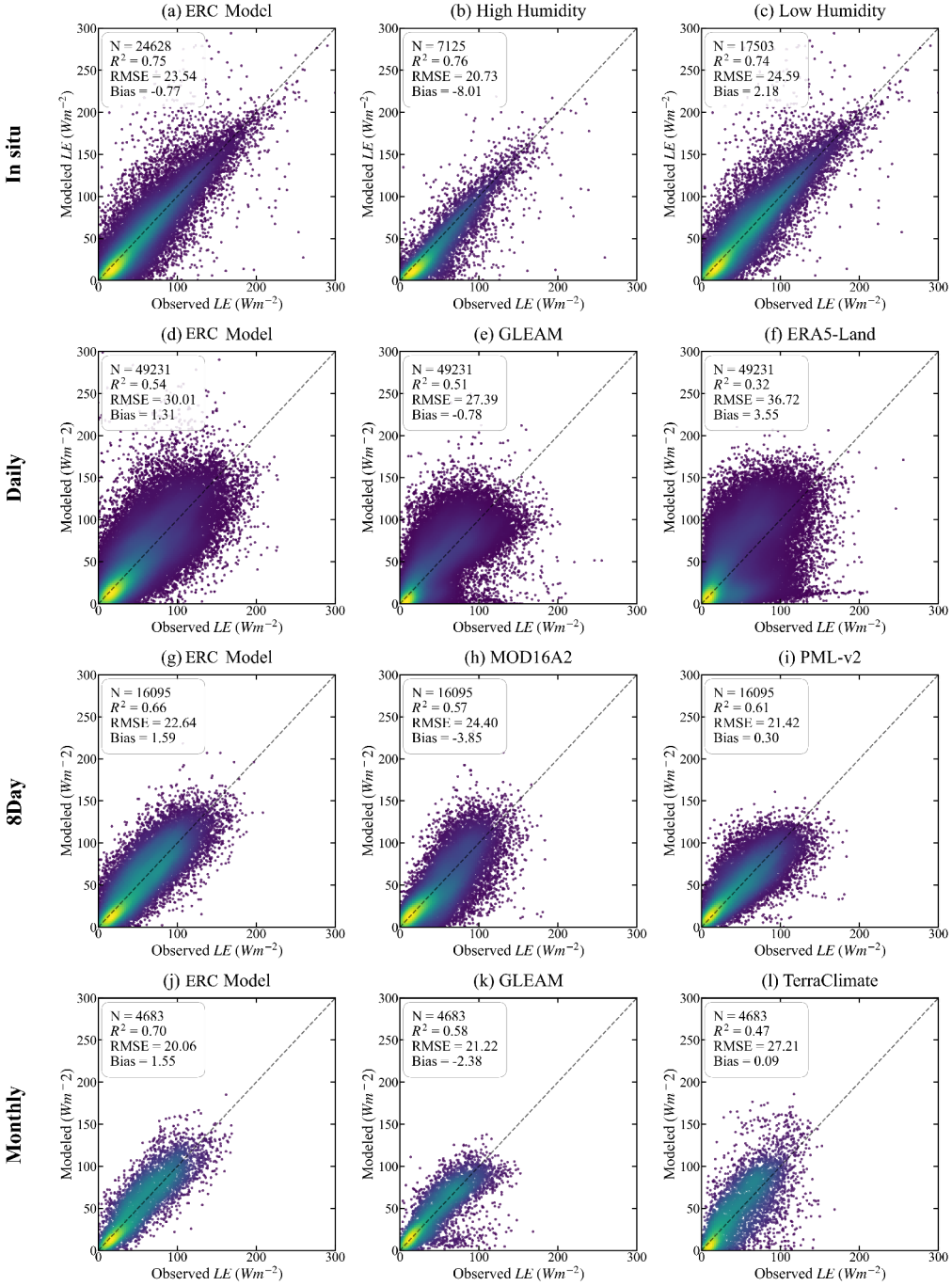
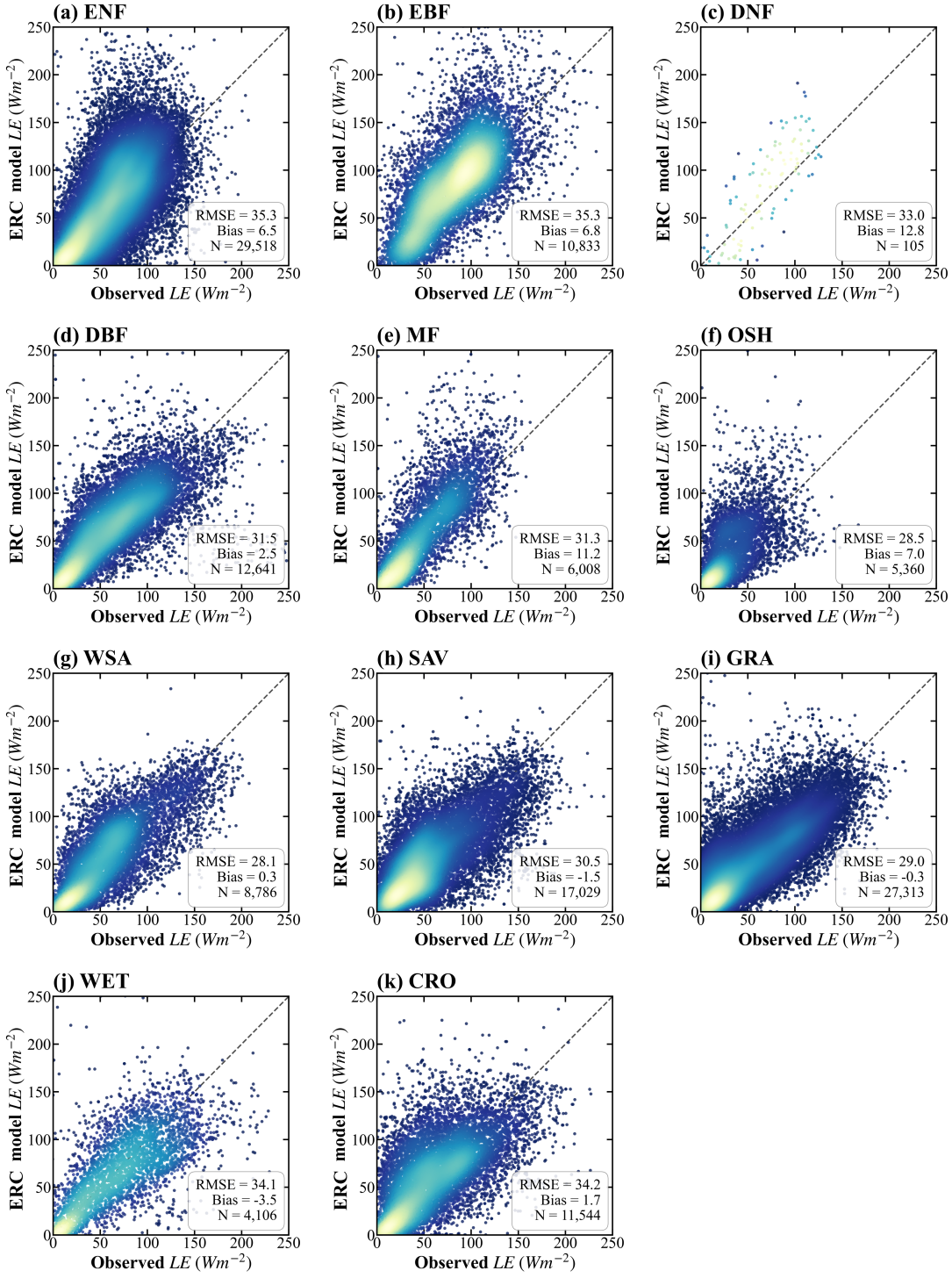


Figure 7: Multi-scale accuracy evaluations and product comparisons of latent heat flux (*LE*). (a–c) Daily-scale validation against in-situ observations across global sites (overall, high-humidity, and low-humidity environments). (d–f) Daily-scale comparison with the GLEAM, ERA5-Land products. (g–i) 8-day scale comparison with the MOD16A2, PML-v2 products. (j–l) Monthly scale comparison with the GLEAM, TerraClimate products.

https://doi.org/10.5194/essd-2026-678
Preprint. Discussion started: 16 November 2026
© Author(s) 2026. CC BY 4.0 License.



285 **Figure 8: Accuracy of the ERC-estimated latent heat flux (*LE*) against in-situ observations across 11 representative land cover types.**

https://doi.org/10.5194/essd-2026-678
Preprint. Discussion started: 16 November 2026
© Author(s) 2026. CC BY 4.0 License.



4.3 Global spatiotemporal characteristics of latent heat flux

Figure 9 brings together the global *LE* fields from ERC, PML-V2, and MOD16A2 for four selected 8-day intervals in 2020. It also includes the long-term mean state and temporal changes derived from the ERC product over 2001–2020. The four observation windows were chosen to represent distinct phases of the annual cycle. Their comparison allows the consistency of global *LE* patterns and seasonal shifts in evaporation to be examined.

Across the four 8-day periods, the three products exhibit broadly consistent global-scale spatial patterns; high LE values are predominantly observed over humid tropical forests, monsoon regions, and seasonally active temperate vegetation, whereas low *LE* occurs over deserts, sparsely vegetated drylands, snow-covered regions, and high-latitude cold areas. The seasonal evolution is well captured by the ERC model. In early January, high *LE* is largely confined to the Southern Hemisphere summer regions and the humid tropics, while northern high latitudes exhibit very low values. In the April composite, LE has already started to rise across several mid-latitude areas of the Northern Hemisphere. This increase coincides with spring vegetation development and the seasonal growth in available energy. In early July, high *LE* expands strongly across eastern North America, Europe, northern India, eastern China, and boreal Eurasia, corresponding to the Northern Hemisphere growing season. By early October, *LE* declines over many northern temperate and boreal regions, while relatively high values persist in tropical and monsoon-influenced areas.

Despite the overall agreement, the 8-day comparisons reveal notable regional differences among the products. PML-V2 generally shows stronger high- *LE* and sharper spatial contrasts in humid tropical and monsoon regions, particularly over the Amazon Basin, Congo Basin, Southeast Asia, and parts of South Asia. MOD16A2 produces smoother and generally lower *LE* values across several regions, especially over some drylands, high-latitude areas, and seasonally active vegetation zones. In contrast, ERC yields a more spatially continuous and moderately constrained pattern, particularly across transition zones between humid and semi-arid regions. These differences are most evident during the growing season, when vegetation phenology, radiation, water availability, and surface resistance exert strong and rapidly changing controls on *LE*. In arid and semi-arid regions, discrepancies among the three products likely stem from different representations of soil moisture limitation, bare-soil evaporation, vegetation water stress, and resistance parameterization. Collectively, these seasonal snapshots demonstrate that ERC reproduces not only the persistent spatial gradients in LE but also its seasonal migration across hemispheres and vegetation zones.

The spatial pattern of multi-year mean ERC LE further reveals a clear latitudinal gradient (Fig. 9m). The highest values are observed over equatorial tropical forests and humid monsoon regions, with progressively lower values toward subtropical drylands and high-latitude cold regions. The corresponding zonal mean confirms the predominant contribution of low-latitude humid regions to global terrestrial LE. The temporal trend shows widespread increases in *LE* over many land areas from 2001 to 2020 (Fig. 9n), especially in parts of the northern mid- to high-latitudes and humid tropical or monsoon regions, while localized decreases occur in some arid and semi-arid regions. The zonal trend profile further indicates that *LE* changes vary strongly with latitude and hydroclimatic conditions.

https://doi.org/10.5194/essd-2026-678
Preprint. Discussion started: 16 November 2026
© Author(s) 2026. CC BY 4.0 License.

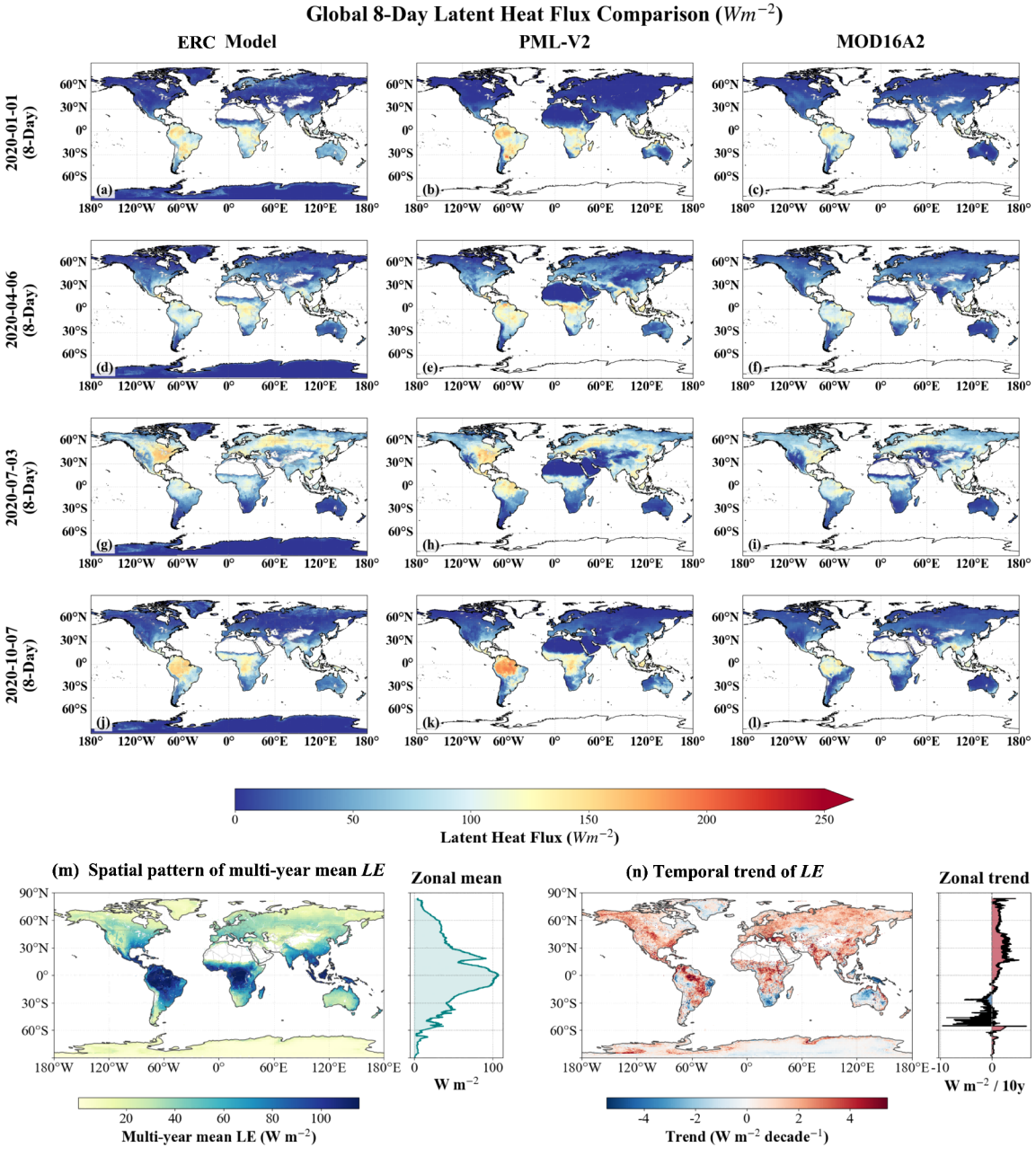


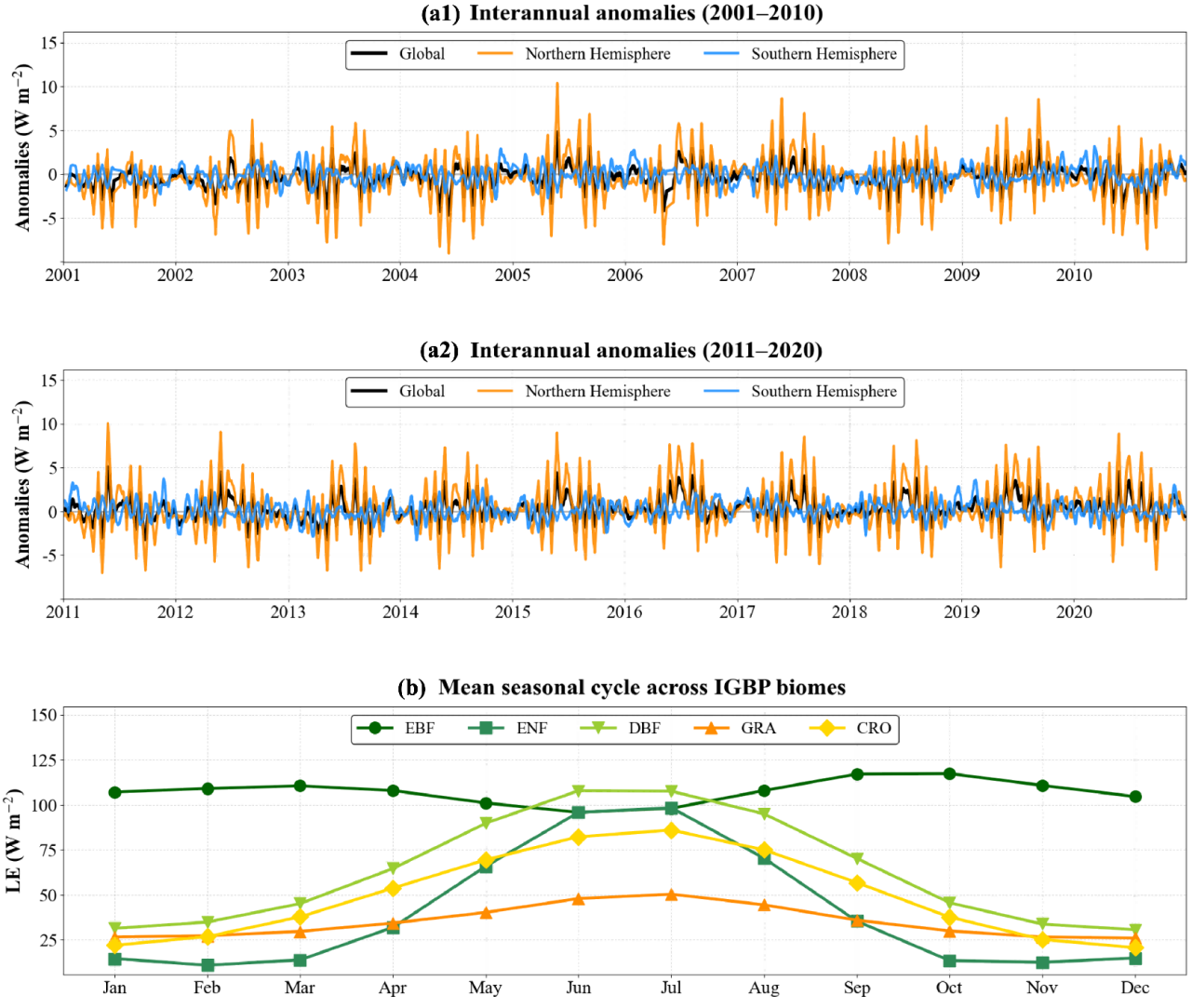
Figure 9: Spatial distribution of global 8-day latent heat flux (*LE*) across four representative periods in 2020. The panels demonstrate the ERC (a, d, g, j), PML-v2 (b, e, h, k), and MOD16A2 (c, f, i, l) products. Blank areas indicate missing pixels. (m) spatial distribution and latitudinal mean profile of multi-year mean LE. (n) Long-term temporal trends and latitudinal profile of ERC LE.

Figure 10 summarizes the long-term temporal characteristics of global *LE* from 2001 to 2020. The interannual anomaly series shows that global *LE* variability is dominated by the Northern Hemisphere (Fig. 10a). The biome-specific seasonal cycles in Fig. 10b further indicate that the ERC dataset captures physically reasonable seasonal variations across different vegetation

https://doi.org/10.5194/essd-2026-678
Preprint. Discussion started: 16 November 2026
© Author(s) 2026. CC BY 4.0 License.



types. Evergreen broadleaf forests (EBF) maintain high *LE* throughout the year, whereas DBF, CRO, and GRA show a pronounced unimodal seasonal cycle with peak *LE* occurring during the Northern Hemisphere summer. These results suggest that the ERC product reflects both hemispheric-scale variability and biome-specific seasonality.



330 **Figure 10: Temporal evolution of global *LE* over the 2001–2020 period. (a1) and (a2) display annual *LE* anomalies at the global scale and for the Northern and Southern hemispheres during 2001–2010 and 2011–2020, respectively. (b) compares the monthly climatological *LE* patterns among the selected IGBP land-cover classes.**

4.4 Global spatiotemporal characteristics of intermediate parameters

Figure 11 presents the global distributions of daily r_{ae}, r_s, Ω, and $h_{s,max}$ for four representative dates in 2020. These variables
335 exhibit coherent spatial and seasonal structures, indicating that the ERC framework captures not only the magnitude of LE exchange but also the underlying resistance and coupling states that regulate land-atmosphere water vapor transfer.

https://doi.org/10.5194/essd-2026-678
Preprint. Discussion started: 16 November 2026
© Author(s) 2026. CC BY 4.0 License.



During the growing season, relatively low r_{ae} values are associated with dense vegetation and high aerodynamic roughness. This spatial pattern is evident across the Amazon and Congo basins, Southeast Asia, as well as vegetated areas of eastern North America, Europe, and eastern China. In contrast, high r_{ae} values are found in high-latitude winter regions, snow-covered or high-elevation areas, and sparsely vegetated drylands, where vertical exchange is limited (Fig. 11a-d).

The spatial variability of r_s reflects both moisture availability and vegetation activity (Fig. 11e–h). Relatively small rs values occur in humid tropical and monsoon-influenced environments, including the Amazon and Congo basins, Southeast Asia, and the monsoon belt of South Asia. In these environments, abundant moisture and active vegetation favor water vapor transfer from the land surface. By contrast, very high r_s values are concentrated over the Sahara, Arabian Peninsula, central Asia, western North America, southern Africa, and inland Australia. These regions are generally associated with strong water limitation and sparse vegetation. High r_s also appears over high-latitude dormant or frozen regions during cold seasons, indicating that the ERC framework captures both humidity-induced and phenology-induced increases in r_s. Compared with r_{ae}, r_s shows sharper contrasts between humid forests and drylands.

The Ω integrates the effects of r_{ae} and r_s and provides a diagnostic indicator of the dominant control on *LE* (Fig. 11i-l). Relatively high Ω values are mainly distributed over humid and densely vegetated regions, including tropical rainforests and summer-active temperate forests. In these regions, low r_s and sufficient moisture supply indicate stronger energy control on *LE*. In contrast, low Ω values occur over deserts, sparse shrublands, semi-arid transition zones, and cold dormant regions, where high r_s and/or inefficient turbulent exchange strengthen the dependence of *LE* on atmospheric demand and surface water limitation. The seasonal increase of Ω over Northern Hemisphere temperate and boreal vegetation in July is consistent with the simultaneous decrease in r_{ae} and r_s, indicating a transition toward more active land-atmosphere water exchange during the growing season.

The pattern of $h_{s,max}$ further constrains the moisture state of the effective evaporating surface (Fig. 11m-p). High $h_{s,max}$ values are mainly found over humid forests and moisture-abundant regions. By comparison, reduced $h_{s,max}$ is associated with dryland environments. These areas extend from the fringes of the Sahara and the continental interior of Asia to western North America, southern Africa, and the Australian interior. Its seasonal evolution is consistent with vegetation and moisture dynamics: humid and growing-season regions maintain higher $h_{s,max}$ whereas drylands and dormant regions show reduced $h_{s,max}$.

Together, the four variables show clear regional contrasts: humid tropical forests generally exhibit low r_{ae}, low r_s, high Ω, and high $h_{s,max}$, whereas arid and semi-arid regions show higher resistance, lower surface humidity, and stronger water limitation. Temperate and boreal regions show stronger seasonal variability. These patterns indicate that the ERC variables provide useful diagnostic information beyond *LE* alone.

https://doi.org/10.5194/essd-2026-678
Preprint. Discussion started: 16 November 2026
© Author(s) 2026. CC BY 4.0 License.

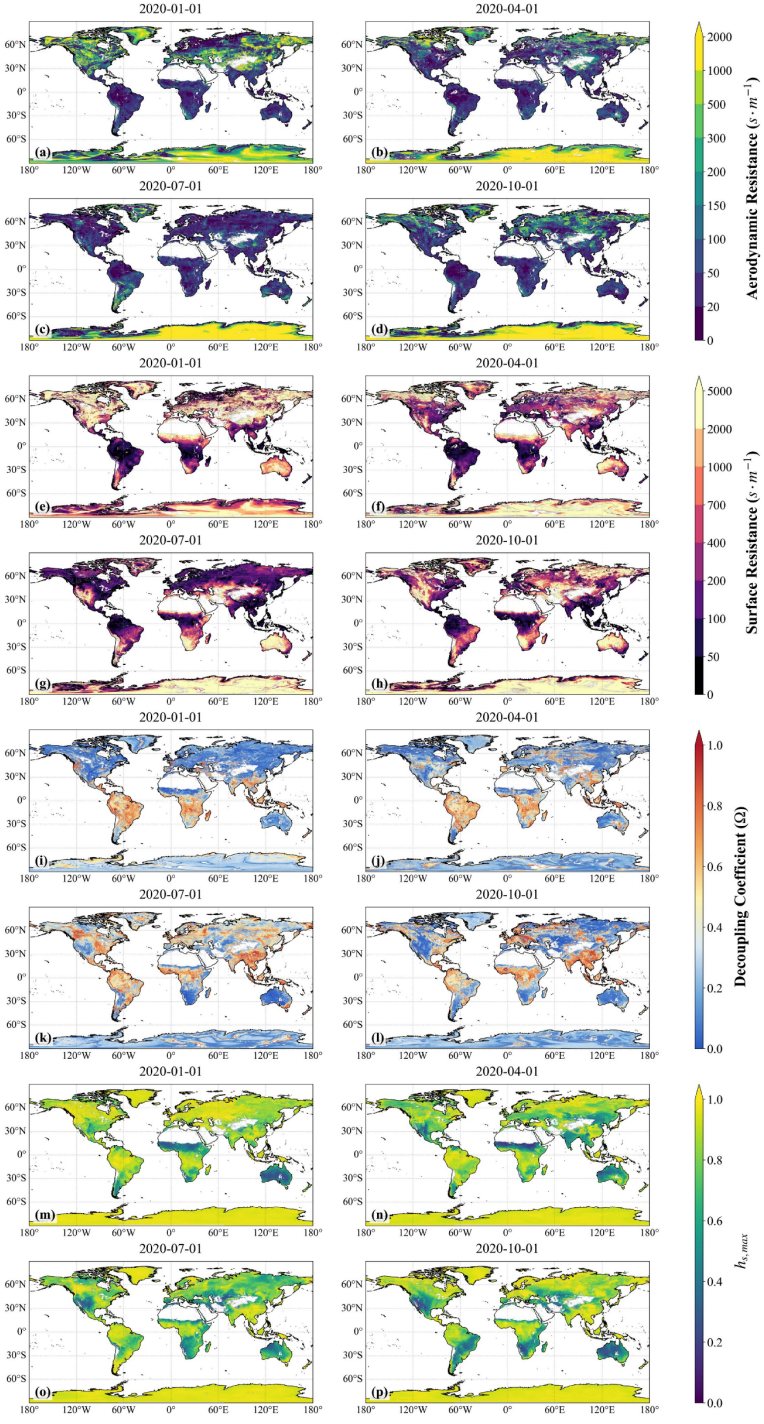


Figure 11: Global daily fields of the ERC-derived variables on four selected dates in 2020 (1 January, 1 April, 1 July, and 1 October). Panels (a–d), (e–h), (i–l), and (m–p) correspond to aerodynamic resistance (r_{ae}), surface resistance (r_s), decoupling coefficient (Ω), and maximum surface relative humidity ($h_{s,max}$). The columns follow chronological order.

https://doi.org/10.5194/essd-2026-678
Preprint. Discussion started: 16 November 2026
© Author(s) 2026. CC BY 4.0 License.

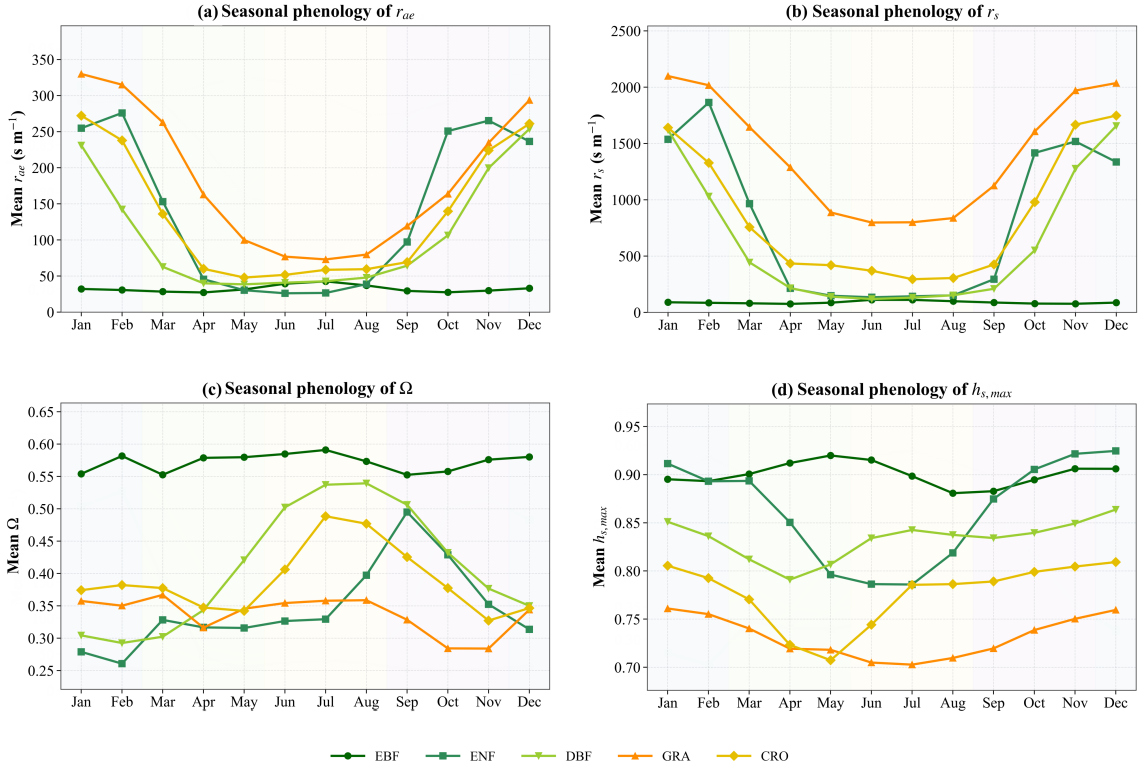


Open Access Earth System Science Data Discussions

370 To investigate biome-dependent seasonal variations in the ERC intermediate variables, we calculated monthly means of r_{ae}, r_s, Ω and $h_{s,max}$ from 2001 to 2020 for five representative IGBP land-cover types, including EBF, ENF, DBF, GRA, and CRO (Fig.12).

The two resistance variables exhibit stronger seasonal amplitudes. Specifically, r_s remains low and stable in EBF, reflecting weak surface limitation under humid evergreen conditions. For ENF, DBF, GRA, and CRO, r_s follows a pronounced U-shaped
375 annual trajectory. Resistance is elevated during the cold season, declines toward midsummer, and subsequently recovers in fall. The seasonal contrast is strongest in GRA and CRO. The annual course of r_{ae} is broadly comparable: its magnitude remains elevated from winter into early spring, followed by a decline as the growing season progresses. The reduction of r_{ae} in summer suggests enhanced turbulent exchange associated with active vegetation, greater surface roughness, and stronger land–atmosphere exchange.

380 The $h_{s,max}$ shows clear biome-dependent differences. In EBF, $h_{s,max}$ maintains consistently high throughout the year, indicating relatively stable humid surface conditions. In ENF, $h_{s,max}$ also shows high values in winter and late autumn, but decreases markedly from spring to summer, suggesting stronger seasonal limitation during the growing season. In DBF, $h_{s,max}$ displays intermediate value, while it exhibits the lowest value in GRA and CRO, especially from late spring to summer. This pattern indicates that grassland are more strongly affected moisture limitation than forests.



385

Figure 12. Monthly climatologies of the four ERC intermediate variables across five representative IGBP land-cover classes for 2001–2020: (a) r_{ae}, (b) r_s, (c) Ω, and (d) $h_{s,max}$. Each curve represents the multi-year monthly mean for one land-cover class.

https://doi.org/10.5194/essd-2026-678
Preprint. Discussion started: 16 November 2026
© Author(s) 2026. CC BY 4.0 License.



The Ω further reveals differences in land-atmosphere coupling among vegetation types. EBF maintains the highest Ω values throughout the year, indicating that LE in these tropical forests is more strongly controlled by available energy and canopy conditions. DBF and CRO show clear increases in Ω during the growing season, consistent with reduced resistance and enhanced canopy activity. ENF exhibits a delayed increase in Ω, while GRA generally maintains lower values, indicating that grassland LE remains more tightly coupled to atmospheric demand and water-stress constraints.

Overall, the ERC intermediate variables capture distinct ecosystem-level seasonal regulation mechanisms. EBF is characterized by persistently high $h_{s,max}$, low r_s and r_{ae}, and high Ω, reflecting stable humid conditions and large LE. In contrast, seasonal vegetation types such as DBF and CRO show strong growing-season reductions in resistance and increases in decoupling, while GRA exhibits stronger moisture limitation. These biome-dependent seasonal patterns provide process-level support for the physical interpretability of the ERC framework and help explain the spatial and seasonal variations in ERC LE.

4.5 Uncertainties

To sum up, the ERC physical iterative framework enabled the generation of a global and spatiotemporally continuous dataset of LE and intermediate parameters. Several sources of uncertainty of course remain and should be considered.

4.5.1 Uncertainties in aerodynamic temperature calibration and sensible heat flux partitioning

Aerodynamic temperature (T_0) is a key input in the ERC framework because it represents the thermal state relevant to turbulent exchange. We derive T_0 empirically from the surface–air temperature contrast, while also accounting for atmospheric stability during calibration. This approach enables large-scale application but simplifies the thermal roughness problem. A one-dimensional formulation may cannot fully represent the mismatch between momentum and thermal roughness over complex canopies, especially when within-canopy transport and sub-canopy heat exchange are not directly observed. Figure 16 provides a tower-based assessment of the modelled H. For the complete evaluation sample, the error statistics were 36.7 W m^{-2} (RMSE), and -17.5 W m^{-2} (bias). Errors varied across land-cover types. The largest errors occurred in forested areas. Evergreen broadleaf forests exhibited an RMSE of 39.7 W m^{-2}, whereas the corresponding value for deciduous broadleaf forests was 45.5 W m^{-2}. Smaller errors were obtained for the less structurally complex vegetation classes. The RMSEs for cropland and grassland were 26.3 and 28.4 W m^{-2}, respectively. These patterns are consistent with the expectation that aerodynamic temperature parameterization is more challenging where canopy structure is vertically complex and thermal stratification is less directly represented by bulk formulations. Importantly, the larger uncertainty in sensible heat flux should not be interpreted as a contradiction of the ERC framework itself. Under a forced-closure solution constrained by the surface energy balance, sensible heat flux tends to absorb part of the residual uncertainty originating from R_n, G and other input variables. The larger uncertainty in sensible heat flux mainly reflects uncertainty redistribution within the energy-closure constraint.

https://doi.org/10.5194/essd-2026-678
Preprint. Discussion started: 16 November 2026
© Author(s) 2026. CC BY 4.0 License.

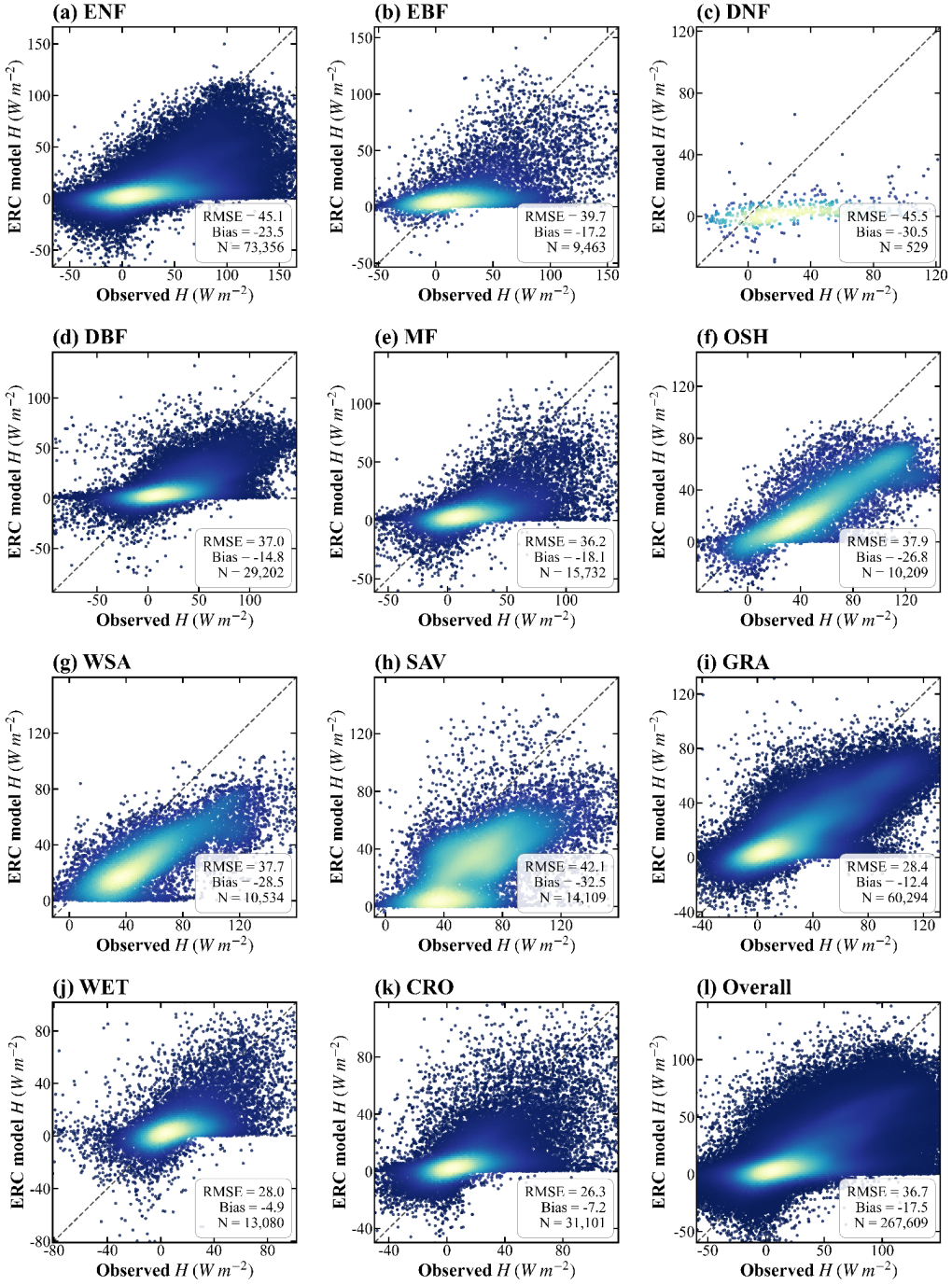


Figure 13: Accuracy of the ERC-estimated sensible heat flux (*H*) against in-situ sites across 11 representative land cover types.

https://doi.org/10.5194/essd-2026-678
Preprint. Discussion started: 16 November 2026
© Author(s) 2026. CC BY 4.0 License.

Open Access Earth System Science Data Discussions

4.5.2 Applicability of the ERC framework to perennial snow and ice

The ERC formulation becomes less suitable in regions that remain covered by snow or ice throughout the year (SNO). The resistance network used here is based on the Penman–Monteith framework and is originally designed for the soil–vegetation–atmosphere continuum. Over snow and ice, surface energy consumption is instead dominated by phase changes, such as melting and sublimation, and by deep thermal storage (Hock, 2005; Cuffey and Paterson, 2010). Under these conditions, stomatal or leaf-boundary-layer resistance concepts become less meaningful, making the classical resistance-network interpretation less appropriate. Consequently, when the ERC solver enforces energy closure over such surfaces, the estimated r_{ae} and r_s may be driven toward unrealistically large values. Rigorous evaluation is difficult because high-quality EC observations over perennial snow and ice are limited; only three SNO sites (US-NGB, SJ-Blv, and GL-Dsk) passed the quality-control procedure, and wintertime flux measurements at these sites remain instrumentally challenging. As a result, both the model formulation and the observational benchmark are weak over SNO surfaces. For this reason, resistance-related estimates over perennial snow and ice should be interpreted with caution.

5 Conclusions

We provide daily global fields at a spatial resolution of 0.05° for the period 2001–2020. The released variables include *LE*, r_{ae}, r_s,Ω, and $h_{s,max}$. The daily estimates were generated through iterative ERC calculations, with satellite observations, meteorological reanalysis, and eddy-covariance measurements supplying the required inputs. The ERC framework integrates three key components: aerodynamic temperature calibration, an XGBoost-based constraint on $h_{s,max}$, and a Newton–Raphson solution of the coupled resistance system. The development of this dataset is motivated by two persistent challenges in large-scale *LE* estimation: existing frameworks often rely on empirical or prescribed resistance parameterizations, and most global products provide only final flux estimates while lacking long-term, spatially continuous datasets of r_{ae} and r_s. Evaluation against 244 globally distributed flux sites indicates that the dataset performs well under both typical hydroclimatic conditions and moisture-stressed environments. In addition to the validation against site observations, comparisons across daily, 8-day, and monthly timescales further show that the ERC product provides competitive performance relative to several widely used global *LE* products. Beyond the *LE* itself, the ERC dataset provides a coherent set of resistance and coupling variables that are rarely available. This makes the dataset valuable not only for *LE* studies, but also for analyses of land–atmosphere coupling, hydroclimatic variability, and drought-related surface processes. Overall, this dataset adds globally consistent information on surface resistance and land–atmosphere coupling. It can support investigations of water–energy interactions and their responses to changing climatic conditions.

https://doi.org/10.5194/essd-2026-678
Preprint. Discussion started: 16 November 2026
© Author(s) 2026. CC BY 4.0 License.



Open Access Earth System Science Data Discussions

Data availability

The global 0.05° ERC dataset generated in this study for 2001–2020 is publicly available through Science Data Bank (ScienceDB) (Zhang et al., 2026). The dataset can be accessed at https://doi.org/10.57760/sciencedb.45211. The dataset will be released in NetCDF format, with one file per day, and each daily file will contain five variables: latent heat flux (*LE*), aerodynamic exchange resistance (r_{ae}), surface resistance (r_s), the decoupling coefficient (Ω), and maximum surface relative humidity ($h_{s,max}$).

The input datasets used in this study are available from their respective providers. The global 1-km all-weather daily mean land surface temperature dataset is available at https://doi.org/10.5281/zenodo.4292067 (Li et al., 2024). The MODIS MAIAC daily NDVI product (MCD19A3CMG.061) and the MODIS land-cover product (MCD12C1.061) can be accessed through NASA's Land Processes Distributed Active Archive Center (LP DAAC) at https://doi.org/10.5067/MODIS/MCD19A3CMG.061 and https://doi.org/10.5067/MODIS/MCD12C1.061, respectively. The GLASS V6 MODIS leaf area index (LAI) product is available through the GLASS data portal (https://glass.hku.hk/download.html; Ma and Liang, 2022; https://doi.org/10.1016/j.rse.2022.112985). ERA5-Land meteorological data are available from the Copernicus Climate Data Store at https://doi.org/10.24381/cds.e2161bac.

The eddy-covariance observations used in this study were obtained from six flux networks and data repositories: AmeriFlux (https://ameriflux.lbl.gov/data/), ChinaFLUX (https://www.chinaflux.org/), the European Fluxes Database (https://www.europe-fluxdata.eu/), FLUXNET (https://data.fluxnet.org/), OzFlux (https://data.ozflux.org.au/), and the National Tibetan Plateau/Third Pole Environment Data Center (https://data.tpdc.ac.cn/). The data were accessed and used in accordance with the data policies and citation requirements of the respective providers.

Author contributions

LZ: methodology, data curation, formal analysis, software, validation, writing the original manuscript, and reviewing and editing. XW: investigation, visualization, formal analysis, and validation. YJ: conceptualization, algorithm development, funding acquisition, supervision, and reviewing and editing. SW: investigation, result interpretation, and reviewing and editing. MS: data curation, result interpretation, and reviewing and editing. CH: reviewing and editing.

Competing interests

The contact author has declared that none of the authors has any competing interests.

https://doi.org/10.5194/essd-2026-678
Preprint. Discussion started: 16 November 2026
© Author(s) 2026. CC BY 4.0 License.

Acknowledgements

We gratefully acknowledge the data providers, site teams, and network coordinators of AmeriFlux, ChinaFLUX, EuroFlux, FLUXNET, OzFlux, and TPDC for maintaining and sharing the site observations used in this study. We also thank the teams responsible for the remote sensing and reanalysis datasets employed in this work, including the GLASS framework, MODIS, MCD12C1, and ERA5-Land. In addition, we acknowledge the developers of GLEAM, TerraClimate, and ERA5-Land, whose products are used for intercomparison and evaluation in this study.

Financial support

This research was supported by the National Natural Science Foundation of China (grants: 42371368).

References

Abatzoglou, J. T., Dobrowski, S. Z., Parks, S. A., and Hegewisch, K. C.: TerraClimate, a high-resolution global dataset of monthly climate and climatic water balance from 1958–2015, Sci. Data, 5, 170191, https://doi.org/10.1038/sdata.2017.191, 2018.

Allen, R. G., Tasumi, M., and Trezza, R.: Satellite-based energy balance for mapping evapotranspiration with internalized calibration (METRIC)—model, J. Irrig. Drain. Eng., 133, 380–394, https://doi.org/10.1061/(ASCE)0733-9437(2007)133:4(380), 2007.

Anderson, M. C., Norman, J. M., Diak, G. R., Kustas, W. P., and Mecikalski, J. R.: A two-source time-integrated model for estimating surface fluxes using thermal infrared remote sensing, Remote Sens. Environ., 60, 195–216, https://doi.org/10.1016/S0034-4257(96)00215-5, 1997.

Ball, J. T., Woodrow, I. E., and Berry, J. A.: A model predicting stomatal conductance and its contribution to the control of photosynthesis under different environmental conditions, in: Progress in photosynthesis research: volume 4 proceedings of the VIIth international congress on photosynthesis providence, rhode island, USA, august 10–15, 1986, edited by: Biggins, J., Springer Netherlands, Dordrecht, 221–224, https://doi.org/10.1007/978-94-017-0519-6_48, 1987.

Bastiaanssen, W. G. M., Menenti, M., Feddes, R. A., and Holtslag, A. A. M.: A remote sensing surface energy balance algorithm for land (SEBAL). 1. Formulation, Journal of Hydrology, 212–213, 198–212, https://doi.org/10.1016/S0022-1694(98)00253-4, 1998.

Beringer, J., Hutley, L. B., McHugh, I., Arndt, S. K., Campbell, D., Cleugh, H. A., Cleverly, J., Resco de Dios, V., Eamus, D., Evans, B., Ewenz, C., Grace, P., Griebel, A., Haverd, V., Hinko-Najera, N., Huete, A., Isaac, P., Kanniah, K., Leuning, R., Liddell, M. J., Macfarlane, C., Meyer, W., Moore, C., Pendall, E., Phillips, A., Phillips, R. L., Prober, S. M., Restrepo-Coupe, N., Rutledge, S., Schroder, I., Silberstein, R., Southall, P., Yee, M. S., Tapper, N. J., van Gorsel, E., Vote, C., Walker, J., and

https://doi.org/10.5194/essd-2026-678
Preprint. Discussion started: 16 November 2026
© Author(s) 2026. CC BY 4.0 License.

Wardlaw, T.: An introduction to the australian and New Zealand flux tower network – OzFlux, Biogeosciences, 13, 5895–5916, https://doi.org/10.5194/bg-13-5895-2016, 2016.

Boegh, E., Soegaard, H., and Thomsen, A.: Evaluating evapotranspiration rates and surface conditions using landsat TM to estimate atmospheric resistance and surface resistance, Remote Sens. Environ., 79, 329–343, https://doi.org/10.1016/S0034-4257(01)00283-8, 2002.

Bruin, H. A. R. D.: A model for the priestley-taylor parameter α, 1–7, https://doi.org/10.1175/1520-0450(1983)022%3C0572:AMFTPT%3E2.0.CO;2, 1983.

Brutsaert, W.: Evaporation into the atmosphere: theory, history and applications, Springer Science & Business Media, 299 pp., 2013.

Chen, T. and Guestrin, C.: XGBoost: a scalable tree boosting system, in: Proceedings of the 22nd ACM SIGKDD International Conference on Knowledge Discovery and Data Mining, 785–794, https://doi.org/10.1145/2939672.2939785, 2016.

Collatz, G. J., Ball, J. T., Grivet, C., and Berry, J. A.: Physiological and environmental regulation of stomatal conductance, photosynthesis and transpiration: a model that includes a laminar boundary layer, Agric. For. Meteorol., 54, 107–136, https://doi.org/10.1016/0168-1923(91)90002-8, 1991.

Cuffey, K. M. and Paterson, W. S. B.: The physics of glaciers, Academic Press, 721 pp., 2010.

Ershadi, A., McCabe, M. F., Evans, J. P., Chaney, N. W., and Wood, E. F.: Multi-site evaluation of terrestrial evaporation models using FLUXNET data, Agric. For. Meteorol., 187, 46–61, https://doi.org/10.1016/j.agrformet.2013.11.008, 2014.

Fisher, J. B., Tu, K. P., and Baldocchi, D. D.: Global estimates of the land–atmosphere water flux based on monthly AVHRR and ISLSCP-II data, validated at 16 FLUXNET sites, Remote Sens. Environ., 112, 901–919, https://doi.org/10.1016/j.rse.2007.06.025, 2008.

Fisher, J. B., Melton, F., Middleton, E., Hain, C., Anderson, M., Allen, R., McCabe, M. F., Hook, S., Baldocchi, D., Townsend, P. A., Kilic, A., Tu, K., Miralles, D. D., Perret, J., Lagouarde, J.-P., Waliser, D., Purdy, A. J., French, A., Schimel, D., Famiglietti, J. S., Stephens, G., and Wood, E. F.: The future of evapotranspiration: global requirements for ecosystem functioning, carbon and climate feedbacks, agricultural management, and water resources, Water Resour. Res., 53, 2618–2626, https://doi.org/10.1002/2016WR020175, 2017.

Foken, T.: The energy balance closure problem: an overview, Ecol. Appl., 18, 1351–1367, https://doi.org/10.1890/06-0922.1, 2008.

Friedl, M. and Sulla-Menashe, D.: MODIS/terra+aqua land cover type yearly L3 global 0.05Deg CMG V061, NASA EOSDIS Land Process. Distrib. Act. Arch. Cent. (DAAC) data set, MCD12C1.061, https://doi.org/10.5067/MODIS/MCD12C1.061, 2022.

Gentine, P., Massmann, A., Lintner, B. R., Hamed Alemohammad, S., Fu, R., Green, J. K., Kennedy, D., and Vilà-Guerau de Arellano, J.: Land–atmosphere interactions in the tropics – a review, Hydrol. Earth Syst. Sci., 23, 4171–4197, https://doi.org/10.5194/hess-23-4171-2019, 2019.

© Author(s) 2026. CC BY 4.0 License.



Hock, R.: Glacier melt: a review of processes and their modelling, Prog. Phys. Geogr.: Earth Environ., 29, 362–391, https://doi.org/10.1191/0309133305pp453ra, 2005.

Humphrey, V., Berg, A., Ciais, P., Gentine, P., Jung, M., Reichstein, M., Seneviratne, S. I., and Frankenberg, C.: Soil moisture–atmosphere feedback dominates land carbon uptake variability | nature, Nature, 592, 65–69, https://doi.org/10.1038/s41586-021-03325-5, 2021.

Jarvis, P. G.: The interpretation of the variations in leaf water potential and stomatal conductance found in canopies in the field, Philos. Trans. R. Soc. Lond., B Biol. Sci., 273, 593–610, https://doi.org/10.1098/rstb.1976.0035, 1976.

Jiang, Y., Jiang, X., Tang, R., Li, Z.-L., Zhang, Y., Huang, C., and Ru, C.: Estimation of Daily Evapotranspiration Using Instantaneous Decoupling Coefficient From the MODIS and Field Data, IEEE Journal of Selected Topics in Applied Earth Observations and Remote Sensing, 11, 1832–1838, https://doi.org/10.1109/JSTARS.2018.2834469, 2018.

Jung, M., Koirala, S., Weber, U., Ichii, K., Gans, F., Camps-Valls, G., Papale, D., Schwalm, C., Tramontana, G., and Reichstein, M.: The FLUXCOM ensemble of global land-atmosphere energy fluxes, Sci. Data, 6, 74, https://doi.org/10.1038/s41597-019-0076-8, 2019.

Kalma, J. D., McVicar, T. R., and McCabe, M. F.: Estimating land surface evaporation: a review of methods using remotely sensed surface temperature data, Surv. Geophys., 29, 421–469, https://doi.org/10.1007/s10712-008-9037-z, 2008.

Kelliher, F. M., Leuning, R., Raupach, M. R., and Schulze, E.-D.: Maximum conductances for evaporation from global vegetation types, Agric. For. Meteorol., 73, 1–16, https://doi.org/10.1016/0168-1923(94)02178-M, 1995.

Li, B., Liang, S., Ma, H., Dong, G., Liu, X., He, T., and Zhang, Y.: Generation of global 1 km all-weather instantaneous and daily mean land surface temperatures from MODIS data, Earth Syst. Sci. Data, 16, 3795–3819, https://doi.org/10.5194/essd-16-3795-2024, 2024.

Li, Z.-L., Tang, R., Wan, Z., Bi, Y., Zhou, C., Tang, B., Yan, G., and Zhang, X.: A review of current methodologies for regional evapotranspiration estimation from remotely sensed data, Sens., 9, 3801–3853, https://doi.org/10.3390/s90503801, 2009.

Lyapustin, A.: MODIS/terra+aqua vegetation index from MAIAC, daily L3 global 0.05Deg CMG V061, NASA EOSDIS Land Process. Distrib. Act. Arch. Cent. (DAAC) data set, MCD19A3CMG.061, https://doi.org/10.5067/MODIS/MCD19A3CMG.061, 2023.

Ma, H. and Liang, S.: Development of the GLASS 250-m leaf area index product (version 6) from MODIS data using the bidirectional LSTM deep learning model, Remote Sens. Environ., 273, 112985, https://doi.org/10.1016/j.rse.2022.112985, 2022.

Ma, H., Liang, S., Xiong, C., Wang, Q., Jia, A., and Li, B.: Global land surface 250 m 8 d fraction of absorbed photosynthetically active radiation (FAPAR) product from 2000 to 2021, Earth Syst. Sci. Data, 14, 5333–5347, https://doi.org/10.5194/essd-14-5333-2022, 2022.

Mahrt, L.: The bulk aerodynamic formulation over heterogeneous surfaces, Boundary Layer Meteorol., 78, 87–119, https://doi.org/10.1007/BF00122488, 1996.

https://doi.org/10.5194/essd-2026-678
Preprint. Discussion started: 16 November 2026
© Author(s) 2026. CC BY 4.0 License.

Mallick, K., Jarvis, A. J., Boegh, E., Fisher, J. B., Drewry, D. T., Tu, K. P., Hook, S. J., Hulley, G., Ardö, J., Beringer, J., Arain, A., and Niyogi, D.: A surface temperature initiated closure (STIC) for surface energy balance fluxes, Remote Sens. Environ., 141, 243–261, https://doi.org/10.1016/j.rse.2013.10.022, 2014.

Martens, B., Miralles, D. G., Lievens, H., van der Schalie, R., de Jeu, R. A. M., Fernández-Prieto, D., Beck, H. E., Dorigo, W. A., and Verhoest, N. E. C.: GLEAM v3: satellite-based land evaporation and root-zone soil moisture, Geosci. Model Dev., 10, 1903–1925, https://doi.org/10.5194/gmd-10-1903-2017, 2017.

Mazdiyasni, O. and AghaKouchak, A.: Substantial increase in concurrent droughts and heatwaves in the United States, Proceedings of the National Academy of Sciences, 112, 11484–11489, https://doi.org/10.1073/pnas.1422945112, 2015.

McNaughton, K. G. and Jarvis, P. G.: Predicting effects of vegetation changes on transpiration and evaporation, in: Additional woody crop plants, Elsevier, 1–47, https://doi.org/10.1016/B978-0-12-424157-2.50007-0, 1983.

Miralles, D. G., Holmes, T. R. H., De Jeu, R. a. M., Gash, J. H., Meesters, A. G. C. A., and Dolman, A. J.: Global land-surface evaporation estimated from satellite-based observations, Hydrol. Earth Syst. Sci., 15, 453–469, https://doi.org/10.5194/hess-15-453-2011, 2011.

Monteith, J. L.: Evaporation and environment, 19, 205–234, 1965a.

Monteith, J. L.: Evaporation and environment, 19, 205–234, 1965b.

Mu, Q., Zhao, M., and Running, S. W.: Improvements to a MODIS global terrestrial evapotranspiration algorithm, Remote Sens. Environ., 115, 1781–1800, https://doi.org/10.1016/j.rse.2011.02.019, 2011.

Muñoz-Sabater, J., Dutra, E., Agustí-Panareda, A., Albergel, C., Arduini, G., Balsamo, G., Boussetta, S., Choulga, M., Harrigan, S., Hersbach, H., Martens, B., Miralles, D. G., Piles, M., Rodríguez-Fernández, N. J., Zsoter, E., Buontempo, C., and Thépaut, J.-N.: ERA5-land: a state-of-the-art global reanalysis dataset for land applications, Earth Syst. Sci. Data, 13, 4349–4383, https://doi.org/10.5194/essd-13-4349-2021, 2021.

Norman, J. M., Kustas, W. P., and Humes, K. S.: Source approach for estimating soil and vegetation energy fluxes in observations of directional radiometric surface temperature, Agric. For. Meteorol., 77, 263–293, https://doi.org/10.1016/0168-1923(95)02265-Y, 1995.

Novick, K. A., Ficklin, D. L., Stoy, P. C., Williams, C. A., Bohrer, G., Oishi, A. C., Papuga, S. A., Blanken, P. D., Noormets, A., Sulman, B. N., Scott, R. L., Wang, L., and Phillips, R. P.: The increasing importance of atmospheric demand for ecosystem water and carbon fluxes, Nat. Clim. Change, 6, 1023–1027, https://doi.org/10.1038/nclimate3114, 2016.

Novick, K. A., Biederman, J. A., Desai, A. R., Litvak, M. E., Moore, D. J. P., Scott, R. L., and Torn, M. S.: The AmeriFlux network: a coalition of the willing, Agric. For. Meteorol., 249, 444–456, https://doi.org/10.1016/j.agrformet.2017.10.009, 2018.

Oki, T. and Kanae, S.: Global hydrological cycles and world water resources, Science, 313, 1068–1072, https://doi.org/10.1126/science.1128845, 2006.

Pastorello, G., Trotta, C., Canfora, E., Chu, H., Christianson, D., Cheah, Y.-W., Poindexter, C., Chen, J., Elbashandy, A., Humphrey, M., Isaac, P., Polidori, D., Reichstein, M., Ribeca, A., van Ingen, C., Vuichard, N., Zhang, L., Amiro, B., Ammann, C., Arain, M. A., Ardö, J., Arkebauer, T., Arndt, S. K., Arriga, N., Aubinet, M., Aurela, M., Baldocchi, D., Barr, A.,

© Author(s) 2026. CC BY 4.0 License.

Beamesderfer, E., Marchesini, L. B., Bergeron, O., Beringer, J., Bernhofer, C., Berveiller, D., Billesbach, D., Black, T. A., Blanken, P. D., Bohrer, G., Boike, J., Bolstad, P. V., Bonal, D., Bonnefond, J.-M., Bowling, D. R., Bracho, R., Brodeur, J., Brümmer, C., Buchmann, N., Burban, B., Burns, S. P., Buysse, P., Cale, P., Cavagna, M., Cellier, P., Chen, S., Chini, I., Christensen, T. R., Cleverly, J., Collalti, A., Consalvo, C., Cook, B. D., Cook, D., Coursolle, C., Cremonese, E., Curtis, P. S., D'Andrea, E., da Rocha, H., Dai, X., Davis, K. J., Cinti, B. D., Grandcourt, A. de, Ligne, A. D., De Oliveira, R. C., Delpierre, N., Desai, A. R., Di Bella, C. M., Tommasi, P. di, Dolman, H., Domingo, F., Dong, G., Dore, S., Duce, P., Dufrêne, E., Dunn, A., Dušek, J., Eamus, D., Eichelmann, U., ElKhidir, H. A. M., Eugster, W., Ewenz, C. M., Ewers, B., Famulari, D., Fares, S., Feigenwinter, I., Feitz, A., Fensholt, R., Filippa, G., Fischer, M., Frank, J., Galvagno, M., et al.: The FLUXNET2015 dataset and the ONEFlux processing pipeline for eddy covariance data, Sci. Data, 7, 225, https://doi.org/10.1038/s41597-020-0534-3, 2020.

Penman, H. L.: Natural evaporation from open water, bare soil and grass, Proc. R. Soc. Lond., A. Math. Phys. Sci., 193, 120–145, https://doi.org/10.1098/rspa.1948.0037, 1948.

Pereira, A. R.: The priestley–taylor parameter and the decoupling factor for estimating reference evapotranspiration, Agric. For. Meteorol., 125, 305–313, https://doi.org/10.1016/j.agrformet.2004.04.002, 2004.

Priestley, C. H. B. and Taylor, R. J.: On the assessment of surface heat flux and evaporation using large-scale parameters, 1972.

Senay, G. B., Bohms, S., Singh, R. K., Gowda, P. H., Velpuri, N. M., Alemu, H., and Verdin, J. P.: Operational evapotranspiration mapping using remote sensing and weather datasets: a new parameterization for the SSEB approach, J. Am. Water Resour. Assoc., 49, 577–591, https://doi.org/10.1111/jawr.12057, 2013.

Seneviratne, S. I., Corti, T., Davin, E. L., Hirschi, M., Jaeger, E. B., Lehner, I., Orlowsky, B., and Teuling, A. J.: Investigating soil moisture–climate interactions in a changing climate: A review, Earth-Science Reviews, 99, 125–161, https://doi.org/10.1016/j.earscirev.2010.02.004, 2010.

Sheffield, J., Wood, E. F., and Roderick, M. L.: Little change in global drought over the past 60 years, Nature, 491, 435–438, https://doi.org/10.1038/nature11575, 2012.

Stewart, J. B.: Modelling surface conductance of pine forest, Agric. For. Meteorol., 43, 19–35, https://doi.org/10.1016/0168-1923(88)90003-2, 1988.

Su, Z.: The surface energy balance system (SEBS) for estimation of turbulent heat fluxes, Hydrol. Earth Syst. Sci., 6, 85–100, https://doi.org/10.5194/hess-6-85-2002, 2002.

Wang, K. and Dickinson, R. E.: A review of global terrestrial evapotranspiration: observation, modeling, climatology, and climatic variability, Rev. Geophys., 50, 2011RG000373, https://doi.org/10.1029/2011RG000373, 2012.

Wang, X., Jiang, Y., Wang, X., Si, M., Lou, Y., and Kou, H.: A remote sensing-based parameterization method for global maximum surface relative humidity with energy balance multivariable coupling and XGBoost model, IEEE Trans. Geosci. Remote Sens., 63, 1–9, https://doi.org/10.1109/TGRS.2025.3641945, 2025.

https://doi.org/10.5194/essd-2026-678
Preprint. Discussion started: 16 November 2026
© Author(s) 2026. CC BY 4.0 License.



Wang, X., Jiang, Y., Zhang, H., Li, Y., Si, M., Lou, Y., and Li, Z.-L.: A synergetic framework for land-atmosphere coupling-based remote sensing inversion of evapotranspiration, surface resistance, and aerodynamic resistance, *J. Hydrol.*, 136225, https://doi.org/10.1016/j.jhydrol.2026.136225, 2026.

Yu, G.-R., Wen, X.-F., Sun, X.-M., Tanner, B. D., Lee, X., and Chen, J.-Y.: Overview of ChinaFLUX and evaluation of its eddy covariance measurement, Agric. For. Meteorol., 137, 125–137, https://doi.org/10.1016/j.agrformet.2006.02.011, 2006.

Yuan, W., Zheng, Y., Piao, S., Ciais, P., Lombardozzi, D., Wang, Y., Ryu, Y., Chen, G., Dong, W., Hu, Z., Jain, A. K., Jiang, C., Kato, E., Li, S., Lienert, S., Liu, S., Nabel, J. E. M. S., Qin, Z., Quine, T., Sitch, S., Smith, W. K., Wang, F., Wu, C., Xiao, Z., and Yang, S.: Increased atmospheric vapor pressure deficit reduces global vegetation growth, Sci. Adv., 5, eaax1396, https://doi.org/10.1126/sciadv.aax1396, 2019.

Zhang, L., Wang, X., Jiang, Y., Wang, S., and Si, M.: A global 0.05° dataset of daily latent heat flux and resistances (2001–2020) derived via the Energy–Resistance–Coupling framework, Version 1, Science Data Bank (ScienceDB), https://doi.org/10.57760/sciencedb.45211, 2026.

Zhang, Y., Peña-Arancibia, J. L., McVicar, T. R., Chiew, F. H. S., Vaze, J., Liu, C., Lu, X., Zheng, H., Wang, Y., Liu, Y. Y., Miralles, D. G., and Pan, M.: Multi-decadal trends in global terrestrial evapotranspiration and its components, Sci. Rep., 6, 19124, https://doi.org/10.1038/srep19124, 2016.

Zhang, Y., Kong, D., Gan, R., Chiew, F. H. S., McVicar, T. R., Zhang, Q., and Yang, Y.: Coupled estimation of 500 m and 8-day resolution global evapotranspiration and gross primary production in 2002–2017, Remote Sensing of Environment, 222, 165–182, https://doi.org/10.1016/j.rse.2018.12.031, 2019.

Zhao, M. and Running, S. W.: Drought-induced reduction in global terrestrial net primary production from 2000 through 2009, Science, 329, 940–943, https://doi.org/10.1126/science.1192666, 2010.

Zhou, S., Williams, A. P., Berg, A. M., Cook, B. I., Zhang, Y., Hagemann, S., Lorenz, R., Seneviratne, S. I., and Gentine, P.: Land–atmosphere feedbacks exacerbate concurrent soil drought and atmospheric aridity, Proc. Natl. Acad. Sci., 116, 18848–18853, https://doi.org/10.1073/pnas.1904955116, 2019.